Spectrochimica Acta Part A: Molecular and Biomolecular Spectroscopy 313 (2024) 124156

Contents lists available at ScienceDirect

Spectrochimica Acta Part A:
Molecular and Biomolecular Spectroscopy

journal homepage: www.journals.elsevier.com/spectrochimica-acta-part-a-molecular-and-biomolecular-spectroscopy

In-depth investigation of the effect of pH on the autofluorescence properties of DPF3b and DPF3a amyloid fibrils

Julien Mignon [a,b,c,*], Tanguy Leyder [a], Denis Mottet [d], Vladimir N. Uversky [e], Catherine Michaux [a,b,c]

[a] Laboratoire de Chimie Physique des Biomolécules, UCPTS, University of Namur, 61 rue de Bruxelles, 5000 Namur, Belgium
[b] Namur Institute of Structured Matter (NISM), University of Namur, 61 rue de Bruxelles, 5000 Namur, Belgium
[c] Namur Research Institute for Life Sciences (NARILIS), University of Namur, 61 rue de Bruxelles, 5000 Namur, Belgium
[d] Gene Expression and Cancer Laboratory, GIGA-Molecular Biology of Diseases, University of Liège, B34, Avenue de l'Hôpital, 4000 Liège, Belgium
[e] Department of Molecular Medicine, USF Health Byrd Alzheimer's Research Institute, Morsani College of Medicine, University of South Florida, Tampa, FL, United States

HIGHLIGHTS

- Autofluorescence (AF) properties of DPF3 amyloid fibrils are sensitive to pH.
- Fibrils display different AF modes defined as violet, deep-blue, and blue-green.
- Red edge shift behaviours allowed to decipher isoform-specific optical features.
- Diversity in AF emitters and photo-selection likely relates to fibrillar morphology.

GRAPHICAL ABSTRACT

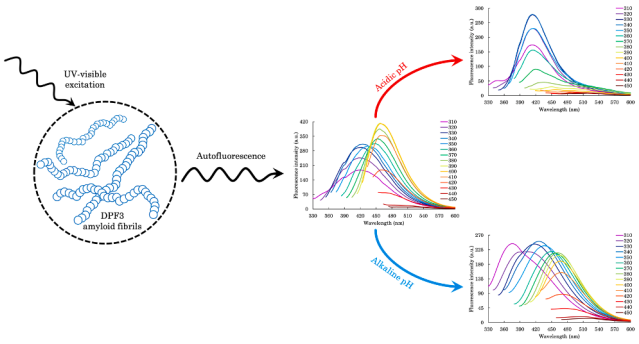

ARTICLE INFO

Keywords:
Double PHD fingers 3 (DPF3)
Amyloid fibril
pH
Deep-blue autofluorescence
Violet autofluorescence

ABSTRACT

Double PHD fingers 3 (DPF3) protein exists as two splicing variants, DPF3b and DPF3a, the involvement of which in human cancer and neurodegeneration is beginning to be increasingly recognised. Both isoforms have recently been identified as intrinsically disordered proteins able to undergo amyloid fibrillation. Upon their aggregation, DPF3 proteins exhibit an intrinsic fluorescence in the visible range, referred to as deep-blue autofluorescence (dbAF). Comprehension of such phenomenon remaining elusive, we investigated in the present study the influence of pH on the optical properties of DPF3b and DPF3a fibrils. By varying the excitation wavelength and the

Abbreviations: APR, aggregation prone region; Alzheimer's disease, AD; AmylPR, amyloid prone region; bgAF, blue-green autofluorescence; BAF, BRM/BRG1-associated factors; CD, circular dichroism; dbAF, deep-blue autofluorescence; DPF3, double PHD fingers 3; FRET, fluorescence resonance energy transfer; ICT, intramolecular charge transfer; ESIPT, excited state intramolecular proton transfer; IDP, intrinsically disordered protein; IPF, intrinsic phenylalanine fluorescence; ITF, intrinsic tryptophan fluorescence; ITyrF, intrinsic tyrosine fluorescence; Parkinson's disease, PD; PHD, plant homeodomain; PBS, phosphate-buffered saline; REES, red edge excitation shift; RTP, room temperature phosphorescence; sw, slit width; TEM, transmission electron microscopy; ThT, thioflavin T; TBS, Tris-buffered saline; vAF, violet autofluorescence; ZnF, zinc finger.

* Corresponding author at: Laboratoire de Chimie Physique des Biomolécules, UCPTS, Université de Namur, rue de Bruxelles 61, 5000 Namur, Belgique.
E-mail addresses: julien.mignon@unamur.be (J. Mignon), tanguy.leyder@unamur.be (T. Leyder), dmottet@uliege.be (D. Mottet), vuversky@usf.edu (V.N. Uversky), catherine.michaux@unamur.be (C. Michaux).

https://doi.org/10.1016/j.saa.2024.124156
Received 12 December 2023; Received in revised form 10 March 2024; Accepted 12 March 2024
Available online 14 March 2024

Blue-green autofluorescence
Red edge excitation shift

pH condition, the two isoforms were revealed to display several autofluorescence modes that were defined as violet, deep-blue, and blue-green according to their emission range. Complementarily, analysis of excitation spectra and red edge shift plots allowed to better decipher their photoselection mechanism and to highlight isoform-specific excitation-emission features. Furthermore, the observed violation to Kasha-Vavilov's rule was attributed to red edge excitation shift effects, which were impacted by pH-mediated H-bond disruption, leading to changes in intramolecular charge and proton transfer, or π-electrons delocalisation. Finally, emergence of different autofluorescence emitters was likely related to structurally distinct fibrillar assemblies between isoforms, as well as to discrepancies in the amino acid composition of their aggregation prone regions.

1. Introduction

Amongst the leading causes of age-related dementia and disability worldwide, Alzheimer's (AD) and Parkinson's diseases (PD) occupy the two top places [1,2]. These two lethal neurodegenerative disorders belong to the class of proteinopathies, characterised by the misfolding and subsequent aggregation of specific proteins, especially within the specific parts of the brain [3,4]. Indeed, while AD pathogenicity relates to the formation of amyloid plaques and neurofibrillary tangles, resulting from the aggregation and accumulation of amyloid β (Aβ) peptide and tau fibers, outside and inside of the neurons, respectively [5], PD mainly arises from the oligomerisation and fibrillation of α-synuclein into proteinaceous inclusions, known as Lewy bodies and Lewy neurites [6]. All these proteins share the ability to conformationally rearrange their intrinsically disordered structure into β-sheets that stack and interact with each other to form the typical cross β-sheet pattern seen in amyloid fibrils [7]. Protein amyloidogenicity is extensively explored *in vitro* by using an array of spectroscopic (e.g. circular dichroism, infrared, and amyloid dye absorption–emission spectroscopy) and microscopic techniques (e.g. confocal, transmission electron, cryogenic electron, and atomic force microscopy) [4], allowing the detection of amyloid-like properties in prone-to-aggregate proteins, which are not necessarily associated with neurodegeneration, such as human insulin, lysozyme, or serum albumin [8–13].

Interestingly, several studies conducted in the last twenty years have highlighted the emergence of a novel intrinsic fluorescence, which seemingly appeared to be related to amyloid fibrillogenesis. By being excited in the UVB to UVA range (280–400 nm), numerous well-described amyloidogenic proteins have shown to exhibit autofluorescence properties, characterised by an emission in the visible range, usually observed between 400 and 490 nm [14–17]. Because of such spectrum, this phenomenon is now more commonly referred to as blue or deep-blue autofluorescence (dbAF). For example, α-synuclein displays, upon its fibrillation, autofluorescence signatures at 425 and 460 nm when respectively excited at 380 and 405 nm [18,19]. The origin of dbAF in fibrillar structures is not substantially studied, and therefore remains poorly understood. Nevertheless, reports have demonstrated that dipolar coupling between excited states of aromatic amino acids [20–22], hydrogen bonds permissive to proton transfer [23–25], change in amide groups communication and geometry through hydrogen bonding [26], charge transport and recombination between charged residues and termini of amyloid proteins [27–31], supramolecular packing and assemblies [32–34], UV- and heat-induced chemical modification of lateral chains such as tyrosine oxidation [15,35–37], as well as quantum confinement effects [21] significantly contribute to the advent of autofluorescence.

Regarding the amyloidogenic proteins, the currently most widely accepted hypothesis proposes that dbAF arises from low-energy electronic transitions due to the delocalisation of peptide π-electrons through the network of hydrogen bonds interconnecting β-strands and -sheets constituting the amyloid cores [15,16,27,38–42]. Such amyloid ordering stabilises n-π* states and hampers non-radiative relaxation thanks to a stiffened network of hydrogen bonding.

It can be pointed out that this type of fluorescence does not essentially require aromatic residues nor multiple bond conjugated systems to occur, and is not exclusive to amyloid material. Indeed, dbAF can be detected, although with lower quantum yields, in non-aggregated and non-amyloid peptides, as well as in standard proteinogenic amino acids and several monomeric proteins, suggesting the further contribution of carbonyl moieties and amide groups to the fluorescence [25,26,28,31,33,42,43]. Furthermore, dbAF is a parameter-dependent phenomenon, as variations of experimental conditions, such as pH [23,44,45], temperature [15,46,47], ionic strength [34], metallic cations [19,37,48,49], solvent and solvation [26,50], or buffer composition [19,20], impact the autofluorescence properties of fibrillated peptides and proteins. Due to the variety of hitherto known autofluorescent proteins, displaying peculiar and distinctive dbAF excitation-emission properties, it is most certain that interactions and structural features being unique to each protein are at work. Indeed, formation of the dbAF-emitting fluorophores and corresponding peculiarities of dbAF are likely protein-specific features. Furthermore, different structural transformations upon aggregation may further tune the optical behaviour of such dbAF emitters.

In the framework of autofluorescent amyloid proteins, we are interested in the double plant homeodomain (PHD) fingers 3 (DPF3) protein, a nuclear zinc finger protein found within the BRM/BRG1-associated factor (BAF) complex, which acts as a chromatin remodeller. Physiopathologically, DPF3 is notably involved in cardiac hypertrophies [51,52], as well as in several cancer types, such as kidney, breast, lung, blood, or brain cancer [53]. Studies suggest that it may also contribute to the development and progression of AD and PD [54–57]. DPF3 exists as two splicing variants, designated as DPF3b and DPF3a. While the two isoforms share a high sequence identity (83%), as well as the same domains organisation up to the 292nd residue, they have distinct C-termini, sequence lengths, and molecular masses. DPF3b and DPF3a are 378 and 357 residues long, and have a molecular mass of 43.08 and 40.24 kDa, respectively. DPF3b sequence ends with a pair of PHD zinc fingers, folded through the coordination of four Zn^{2+} cations. Such PHD tandem is characteristic of the DPF (D4) protein family and recognises acetylated and/or methylated lysine residues on histone tails. On the contrary, the isoform DPF3a has a truncated PHD tandem, as well as a disordered C-terminal end. Despite such primary structure discrepancies, both DPF3b and DPF3a have proved to be intrinsically disordered proteins (IDPs) presenting a propensity to aggregate [58,59].

In our previous studies, we have indeed unveiled the amyloidogenic nature of the two DPF3 isoforms and their respective C-terminal region [49,58,59]. Amongst the spectral fingerprints standardly observed for amyloidogenic proteins, DPF3 isoforms and C-termini have most remarkably revealed to exhibit unique dbAF signatures upon amyloid fibrillation. Strikingly, increase in autofluorescence emission intensity correlates with more efficient thioflavin T (ThT) binding and follows the typical three-phase sigmoid-like kinetic profile of fibril growth. Supported by transmission electron microscopy (TEM) micrographs, these results allowed us to assert that, in the case of the DPF3 proteins, the emergence of dbAF is amyloid-related. Intriguingly, autofluorescence bands also appear on intrinsic tryptophan (ITF) and tyrosine fluorescence (ITyrF) spectra. Comparison of ITF and ITyrF with dbAF excitation spectra, the latter disclosing a contribution in the 260–290 nm vicinity, evidenced that aromatic residues are most likely involved in the DPF3 autofluorescence. More specifically, in our most recent research article,

we have unveiled that DPF3 dbAF is dramatically affected by the presence of diverse divalent metal cations, such as Cu^{2+} and Zn^{2+} [49]. Notably, fibrils of DPF3a C-terminus had their dbAF emission band significantly red-shifted. Cu^{2+} and Zn^{2+} cations also altered the excitation contributions to DPF3a autofluorescence.

In the present study, we investigate the pH-dependent sensitivity of DPF3b and DPF3a amyloid fibrils dbAF to assess the effect of disrupting the protons network and charge state on their fluorescence properties, as well as to better decipher the origin of autofluorescence in DPF3 isoforms.

2. Materials and methods

2.1. Overexpression and purification of recombinant DPF3 isoforms

Human recombinant full-length DPF3 protein isoforms (DPF3b and DPF3a) were tagged with GST at the N-terminus position using a pET-like vector transformed in *E. coli* BL21 Rosetta (DE3) cells. Bacterial strains were grown at 37 °C for approximately 16 h in 20 g/L lysogeny Lennox broth (LB) containing 0.36 mM ampicillin. From the precultures, bacteria were cultured in 20 g/L LB with 0.14 mM ampicillin at 37 °C until the optical density at 600 nm reached a value ranging from 0.5 to 0.8. DPF3 expression was induced at 37 °C for 4 h by adding 0.5 mM isopropyl β-D-1-thiogalactopyranoside (IPTG). Cultures were centrifuged, pelleted, and stored at −20 °C. Upstream from the purification, pellets were thawed at room temperature, suspended in lysis buffer (phosphate-buffered saline (PBS) pH 7.3, 0.5% Triton X-100, 200 mM KCl, 200 μM phenylmethylsulphonyl fluoride), and sonicated in an ice-water bath (6 times 30 s with 30 s pauses). Resulting lysates were centrifuged, supernatants were retrieved and purified using an Äkta Purifier fast protein liquid chromatography. GST-fused DPF3 proteins were bound to a 5 mL GSTrap FF pre-packed column (Cytiva) with the binding buffer (PBS pH 7.3, 200 mM KCl) before being cleaved on column for 2 h at 30 °C in the presence of 20 μL of TEV protease solution (Sigma) in Tris-buffered saline (TBS; 50 mM Tris-HCl pH 8.0, 150 mM NaCl). Cleaved DPF3 proteins were eluted and collected in TBS. The purity and composition of obtained samples were assessed by sodium dodecyl sulphate polyacrylamide gel electrophoresis and mass spectrometry.

2.2. Protein concentration determination

After purification, DPF3 isoforms were further concentrated in TBS through a 6–8 kDa cut-off dialysis membrane wrapped in water-absorbent PEG-20000. UV–visible spectra were recorded between 200 and 400 nm by 1.0 nm increment with a UV-63000PC spectrophotometer (VWR), using a 10 mm optical pathlength quartz QS cell (Hellma). On the basis of the method described by Kuipers B. and Gruppen H. [60], the molar extinction coefficient at 214 nm of each isoform was calculated ($\varepsilon_{DPF3b} = 763132\ M^{-1}.cm^{-1}$, $\varepsilon_{DPF3a} = 622615\ M^{-1}.cm^{-1}$), and the protein concentration was determined with the absorbance value at 214 nm extracted from obtained spectra.

2.3. Amyloid fibril formation and protein sample preparation

DPF3b and DPF3a amyloid fibrils were prepared by incubating 5 μM of purified and concentrated protein material in TBS at ~20 °C for 168 h. Formation of fibrils was monitored and confirmed by far-UV circular dichroism spectroscopy (CD), ThT fluorescence, dbAF, as well as TEM. For each isoform, the stock suspension of fibrils was divided into six samples, three of which were acidified from pH 8 to pH 2, 4, and 6 with 1 M and 1 mM HCl solutions, while two were basified to pH 10 and 12 with 1 M and 1 mM NaOH solutions.

2.4. Assessment of amyloid fibril integrity

To evaluate the integrity and amyloid character of acidified and basified fibrils, far-UV CD and ThT binding assay were carried out for each DPF3 isoform at ~20 °C in TBS. Far-UV CD spectra were recorded with a MOS-500 spectropolarimeter, using a 1 mm optical pathlength quartz Suprasil cell (Hellma) and the following parameters: 60 nm/min scanning rate, 2 nm bandwidth, 0.5 nm data pitch, and 0.5 s digital integration time. Four scans were averaged, buffer baselines were subtracted, and resulting corrected spectra were smoothed. Regarding the ThT binding assay, ThT working solution (80 μM) was prepared in TBS and filtered on polyether sulfone 0.2 μm. After mixing 75 μL of ThT working solution with 75 μL of fibrils (final ThT concentration of 40 μM), fluorescence spectra were recorded with an Agilent Cary Eclipse fluorescence spectrophotometer, using a 10 mm optical pathlength quartz QS cell (Hellma) and the following parameters: 1.0 nm data pitch, 0.1 s averaging time, a photomultiplier tube (PMT) voltage of 600 V, and 600 nm/min scanning rate. Excitation and emission slit widths (sw) were both set to 10 nm. Presented spectra were smoothed.

2.5. Intrinsic fluorescence spectroscopy

After pH adjustment, intrinsic phenylalanine fluorescence (IPF), ItyrF, ITF, and autofluorescence signatures were recorded for each DPF3 isoform with an Agilent Cary Eclipse fluorescence spectrophotometer at ~20 °C in TBS, using a 10 mm optical pathlength quartz QS cell (Hellma) and the following parameters: 1.0 nm data pitch, 0.1 s averaging time, 10 nm excitation-emission sw, 600 V PMT voltage, and 600 nm/min scanning rate. For the fluorescence of aromatic residues, emission scans were performed from the excitation wavelength (260, 275, and 295 nm for IPF, ITyrF, and ITF, respectively) up to 600 nm. Acquisition of autofluorescence spectra was carried out from the excitation wavelength, ranging from 310 to 450 nm by increment of 10 nm, up to 600 nm. Complementarily to emission scans, autofluorescence excitation spectra were also recorded from 200 nm up to the selected maximum emission wavelength ranging, by increment of 10 nm, from 400 to 500 nm. Raman scattering of water was removed through the use of excitation and emission filters and the recording of the blank buffer spectra. Presented spectra were smoothed.

2.6. Time-resolved room temperature phosphorescence

After pH adjustment, time-resolved room temperature phosphorescence (RTP) decay profiles were recorded for each DPF3 isoform with an Agilent Cary Eclipse fluorescence spectrophotometer at ~20 °C in TBS, using a 10 mm optical pathlength QS cell (Hellma). For phosphorescence detection, a high sensitivity PMT voltage of 800 V was applied, excitation-emission sw were set to 20 nm, and the following parameters were used: 0 μs delay time, 1 μs gate time, 5 flashes prior to emission recording, and 1 ms total decay time. Five cycles were averaged and the resulting mean decay curves, after the excitation pulse, were each fitted to a single exponential decay function implemented in the OriginPro (Origin Lab) software and of equation: $I = I_0 + Ae^{(-t/\tau)}$, where I is the RTP intensity, A is the amplitude, t is time, and τ is the lifetime. RTP lifetimes (τ) were extracted from the exponential fits.

2.7. Bioinformatics analyses and predictions

Sequence-based analyses and predictions were performed from the amino acid sequence of each full-length human DPF3 isoform: DPF3b (Uniprot ID: Q92784-1) and DPF3a (Uniprot ID: Q92784-2). Models of the tertiary structure of DPF3 isoforms were generated through the combined approach of MMseqs2-AlphaFold2 available on the ColabFold platform [61,62]. In each case, the first ranked relaxed model was selected for further structural representation and electrostatics calculation.

To examine the effect of pH on the overall charged state of DPF3, pK_a of ionisable groups and isoelectric point (pI) values of DPF3 isoforms were first calculated with PROPKA 3.2 [63,64]; pI varies from 6.09 (folded state) to 6.43 (unfolded state), and 6.58 to 6.73 for DPF3b and DPF3a, respectively. Afterwards, PDB files of selected DPF3 MMseqs2-AlphaFold2 models were prepared for continuum solvation calculations at each pH condition in AMBER force field with the PDB2PQR software [65,66]. Finally, the Adaptive Poisson-Boltzmann Solver (APBS) software suite [66,67] was used for solving the equations of continuum electrostatics at 293.15 K and in the presence of 150 mM NaCl to better emulate the experimental conditions. The radii for Na^+ and Cl^- ions were set to 1.1 and 1.7 Å, respectively. All calculation steps were achieved via the APBS/PDB2PQR website [68]. The resulting Poisson-Boltzmann electrostatic potentials were mapped on the van der Waals surface of DPF3 isoforms model, using a potential scale ranging from -3 k_BT/e to $+3$ k_BT/e.

Residues involved in aggregation prone regions (APRs) and in the formation of amyloid cores, that is, amyloid prone regions (AmylPRs), were defined by combining the sequence-based predictions from FuzPred [69] and FuzDrop [70], and using a selection criterion of a window of at least 5 successive amino acids. Based on these predictions, APRs and AmylPRs were numbered and highlighted for each DPF3 isoform on the corresponding primary structure and MMseqs2-AlphaFold2 model. Furthermore, composition of each APR and AmylPR in negatively (aspartate and glutamate) and positively charged (lysine and arginine), polar (serine, threonine, cysteine, histidine, asparagine, and glutamine) and aromatic residues (phenylalanine, tyrosine, and tryptophan) was plotted with respect to their relative abundance in such regions.

3. Results and discussion

3.1. Effect of pH on the amyloid integrity of DPF3b and DPF3a fibrils

Priorly to the investigation of their autofluorescence signatures, the effect of acidic and alkaline pH on the amyloid character of the fibrils of both DPF3 isoforms was monitored by far-UV CD (Fig. S1) and ThT binding assay (Fig. S2). Upon fibrillation, DPF3b (Fig. S1A) and DPF3a (Fig. S1B) typically exhibit fingerprints of twisted and antiparallel β-sheets with a minimum at 224–226 nm. While the negative band remains centred towards 225 nm, slight changes in shape and intensity can be seen between the different pH conditions. Interestingly, the most noticeable difference manifests at the level of the positive band, the position of which is also characteristic of structured β-sheet elements. The global same trend is observed for the two isoforms. The band is shifted to shorter or longer wavelengths at low or high pH values, respectively; in both cases, the band intensity is also decreased. Subtle variations in the negative and positive bands argue towards subtle local modifications in the β-sheets network, which, however, do not lead to a destabilisation of and loss in β-sheets. Overall, far-UV CD results indicate that the β-sheeted core of DPF3b and DPF3a amyloid fibrils is preserved upon pH variation.

Regarding ThT fluorescence, pH does not significantly impact the emission properties of ThT alone (Fig. S2A). More discrepancies are detected in the presence of DPF3b (Fig. S2B) and DPF3a fibrils (Fig. S2C), which nonetheless display an amyloid positive response to ThT at around 485 nm, regardless of the condition. With the exception of pH 4, pH values below 8 induce a net increase in ThT fluorescence intensity for DPF3b. Regarding DPF3a, alkaline pH slightly increases the ThT emission intensity, while it is decreased at acidic pH. These differences in intensity may be informative on isoform-specific morphological features, as well as on the modulation of ThT binding sites on the surface of the fibrils, the accessibility of which would be influenced by pH, rather than the disassembly of the amyloid cores. Coherently with far-UV CD, the amyloid integrity of the two DPF3 isoforms is confirmed to be maintained, as ThT still binds to their acidified and basified fibrils.

3.2. Autofluorescence properties of DPF3b fibrils at pH 8

To identify pH-dependent variations in the optical behaviour of DPF3b amyloid fibrils, autofluorescence emission was scanned with respect to the excitation wavelength in the range from 310 to 450 nm (Fig. 1). As fibrils were formed and grown under pH 8, the corresponding spectra were selected as reference for comparison with the spectra measured at other tested pH values. At the initial fibrillation conditions, striking spectral changes are already observed (Fig. 1D). By increasing the excitation wavelength from 310 to 400 nm, the dbAF band progressively increases in intensity and shifts to the red, from 420 to 460 nm, with the maximum reached at a λ_{ex} of 390–400 nm. Such bathochromic transition is even more noticeable on normalised emission spectra (Fig. 2D). Contrary to the intensity changes, the displacement in band position is discontinuous. While no shift happens when emission is excited between 310 and 330 nm, the moderate shift in the position of emission spectra begins at excitation at 340 nm before becoming more pronounced at excitation from 350 nm to 380 nm. There is no further displacement of the band in the range where the emission maximum (460 nm) is located, that is, between λ_{ex} of 390 and 420 nm. At longer excitation wavelengths, the intensity rapidly decreases, leading to the disappearance of well-defined emission bands beyond excitation at 430 nm.

The bathochromic shift upon increasing the excitation wavelength is a singular event as it disobeys the Kasha's rule. The latter states, to cite M. Kasha himself, that "the emitting level of a given multiplicity is the lowest excited level of that multiplicity" [71]. In other words, a fluorescence photon can only be emitted from the vibrational ground state of the lowest-energy excited singlet electronic level, irrespectively to the initial excitation level, due to nonradiative processes such as internal conversion and vibrational relaxation [71,72]. However, exceptions to Kasha's rule are not that uncommon, especially in the field of protein fluorescence. Indeed, it has been shown that ITF can distinguish the solvent exposure state of Trp residues upon varying the excitation wavelength from 280 nm to 305 nm. Emission of buried Trp residues protected from bulk water molecules was found to progressively shift to the red by increasing the excitation wavelength [73,74]. Such red edge shifts have also been used as a means to characterise the conformational ensemble of proteins, helping to discriminate folded from molten globule and unfolded states [75].

More interestingly, several studies dealing with the aggregation-mediated dbAF of proteins, peptides, as well as amino acids have reported similar bathochromic effects, which do not comply with the Kasha's rule [20,31,33,50,76,77]. Furthermore, it can be pointed out that dbAF spectra of DPF3b fibrils do not obey the Vavilov's rule either, describing that the quantum yield of fluorescence is independent of the excitation wavelength [78]. Intensity of dbAF indeed varies for each λ_{ex} (Fig. 1D), which has already been detected for other amyloid(-like) aggregates and is often accompanied by anti-Kasha emission, thus breaking the Kasha-Vavilov's rule by extension [33,50,76,77,79,80].

Violation of Kasha's law in such protein systems and assemblies has mainly been attributed to the red edge excitation shift (REES) phenomenon. REES is defined as the shift to higher wavelengths of the emission maximum, induced by a displacement of the excitation wavelength towards the long-wavelength or red edge of the absorption spectrum. Fluorophore excitation is characterised by changes in the dipole moment, followed by the reorganisation of solvent (e.g. water) molecules surrounding the excited fluorophore. In a fully solvated medium, the solvent dipolar relaxation occurs within the time-frame of the excited state life-time (or emission life-time). Conversely, in a rigidified environment, such as in folded or aggregated proteins, water molecules interacting with the fluorophore, i.e. the protein, lose mobility and their dipole moment relaxes at a slower rate than the life-time of the excited state. By exciting at lower energy, namely to the red edge of spectrum, a fluorophore population, around which water dipoles are reoriented to decrease the energy gap between the ground (at a higher energy) and the

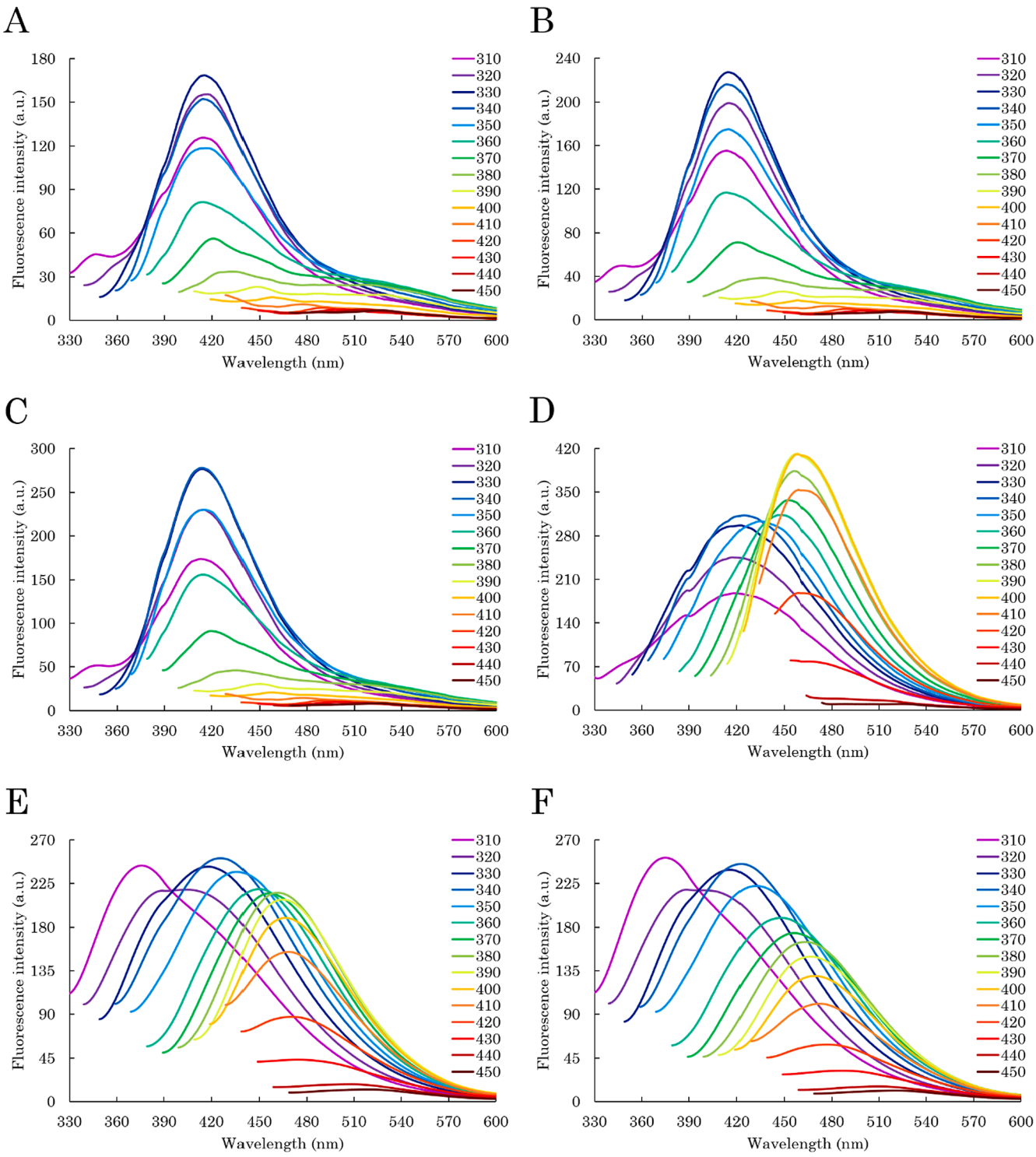

Fig. 1. Autofluorescence emission spectra of full-length DPF3b amyloid fibrils formed in TBS at ~20 °C (C_{DPF3b} = 5 μM) and adjusted to pH values of (A) 2, (B) 4, (C) 6, (D) 8, (E) 10, and (F) 12 upon excitation ranging from 310 to 450 nm (310 ≤ λ_{ex} ≤ 450 nm, sw = 10 nm); 310 (magenta), 320 (purple), 330 (dark blue), 340 (blue), 350 (light blue), 360 (turquoise), 370 (green), 380 (khaki), 390 (lime), 400 (ochre), 410 (orange), 420 (red), 430 (scarlet), 440 (crimson), and 450 nm (merlot).

excited (at a lower energy) states, can be photoselected. Photoselection of fluorophores in such a solvent-relaxed environment hence leads to a red-shifted emission [73,75,81,82]. Occurrence of REES is coherent with water molecules trapped in the cross β-sheet structure of aggregates, as amyloid fibrils are sometimes depicted as 'water-filled nanotubes', and water plays crucial roles in the amyloid formation [83,84]. In that respect, DPF3b fibrils at pH 8 observe an anti-Kasha-Vavilov dbAF emission with respect to the excitation wavelength due to REES, which likely originates from the water molecules interacting at the fibril surface and/or entrapped in the amyloid core.

Giving the position of the emission wavelength in the 310–350 nm λ_{ex} range, dbAF nomenclature needs to be refined. Indeed, λ_{em} between 420 and 440 nm do not localise in the deep blue/blue segment (440–480 nm) of the visible electromagnetic spectrum and correspond instead to violet light. As such, it is more appropriate to refer to the intrinsic fluorescence in this λ_{em} range (380–440 nm) as violet

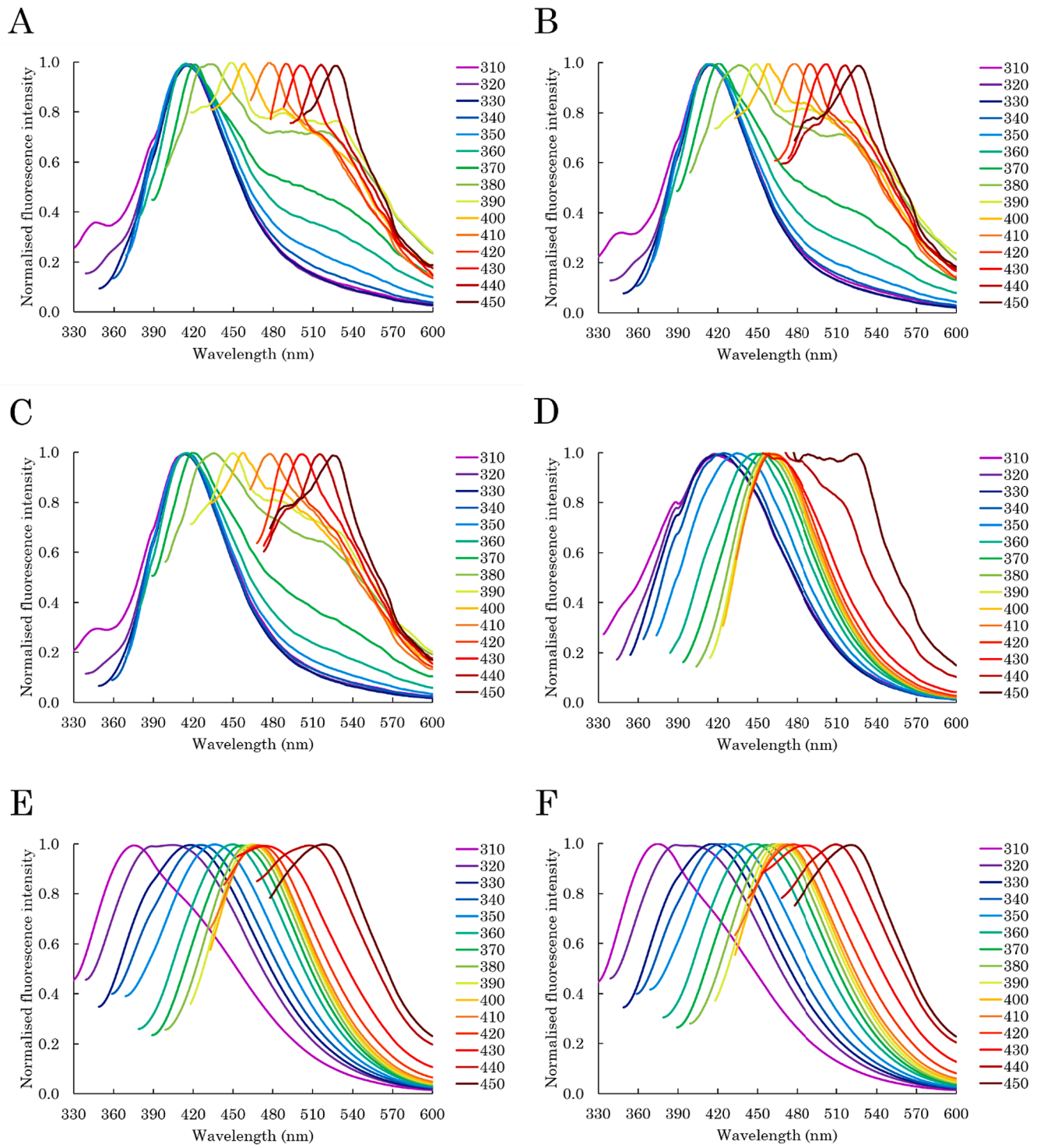

Fig. 2. Normalised autofluorescence emission spectra of full-length DPF3b amyloid fibrils formed in TBS at ~20 °C (C_{DPF3b} = 5 μM) and adjusted to pH values of (A) 2, (B) 4, (C) 6, (D) 8, (E) 10, and (F) 12 upon excitation ranging from 310 to 450 nm (310 ≤ λ_{ex} ≤ 450 nm, sw = 10 nm); 310 (magenta), 320 (purple), 330 (dark blue), 340 (blue), 350 (light blue), 360 (turquoise), 370 (green), 380 (khaki), 390 (lime), 400 (ochre), 410 (orange), 420 (red), 430 (scarlet), 440 (crimson), and 450 nm (merlot).

autofluorescence (vAF). Therefore, DPF3b fibrils display two major autofluorescence modes upon varying their excitation wavelength: vAF (λ_{ex} 310–350 nm) and dbAF (λ_{ex} 360–420 nm). Because the maximum λ_{em} is reached at a λ_{ex} of 390–400 nm, in this case, dbAF dominates over vAF. Existence of such dual emission mode most likely arises from specific structural features and interactions (e.g. dipolar coupling, hydrogen bonding, electron delocalisation, proton and charge transfer, or supramolecular packing) within DPF3b fibrils allowing the emergence of peculiar optical properties, such as red edge shifts.

Apart from REES, the observed autofluorescence λ_{ex}-λ_{em} dependency can also be attributed to multiple photoinduced intramolecular charge transfer (ICT) and recombination between charged amino acids, consequently impacted by (de)protonation of the amyloid core upon pH variation [31,85]. This is not only in good agreement with the

composition of predicted amyloid prone regions (AmylPRs) of DPF3b enriched in polar and charged residues (Fig. S7), but also with the recorded autofluorescence spectra of fibrillated DPF3b at the acidic and basic conditions.

3.3. Effect of acidic pH on the autofluorescence properties of DPF3b fibrils

By lowering the pH to 2, 4, and 6, remarkable and comparable spectral changes are noticed (Figs. 1A–C). The overall emission intensity decreases with pH and the maximum λ_{em} is blue-shifted from 460 to 415 nm. The excitation leading to the emission maximum (415 nm) is found at 330 nm (as well as 340 nm at pH 6). Such a large hypsochromic shift in excitation and emission wavelengths indicates that DPF3b fibrils placed in a more acidic environment preferentially exhibit a more energetic autofluorescence mode and transition from dbAF to a prevalent vAF. After reaching the emission maximum, the autofluorescence intensity rapidly tumbles, so much so that excitation beyond 380 nm only leads to weakly fluorescent populations with barely distinguishable bands. Furthermore, a second autofluorescence band of low quantum yield appears from excitation at 350–360 nm and is even more evident on the normalised spectra (Figs. 2A–C). The latter reveal that, contrary to pH 8, Kasha's rule is obeyed over a wider range of λ_{ex} (310–360 nm), resulting in fixed emission at 415 nm. From 370 up to 450 nm, the maximum λ_{em} is continuously shifted towards 525–527 nm.

Once more, regarding the λ_{em} values obtained at high excitation wavelengths for acidified DPF3b fibrils, a novel autofluorescence mode should be defined. Whilst vAF and dbAF are observed below 410 nm of excitation, emission occurring between 480 and 530 nm rather corresponds to blue-green autofluorescence (bgAF). Therefore, DPF3b fibrils in acidic conditions are characterised by a triple vAF-dbAF-bgAF autofluorescence mode, for which more energetic anti-Vavilov vAF-emitting excited states coexist with a much weaker population of anti-Kasha-Vavilov dbAF- and bgAF-emitting fluorophores.

Major vAF mode obeying Kasha's rule suggests both (de)stabilisation of REES-resistant ground and excited states, involving the release of enclosed and/or interacting water molecules, as well as hindering of ICT due to a modified charged state of the amyloid core, supported by the variation of Poisson-Boltzmann electrostatic potential at the surface of DPF3b (Figs. 4 and S4). By lowering the pH, DPF3b progressively becomes positively charged, especially towards the N-terminal region, where most AmylPRs are found (Fig. S6). Amongst them, AmylPR-3 and -4 are particularly enriched in Asp and Glu residues (Fig. S7). A similar enrichment is observed in AmylPR-6, located in the C-terminal segment, the protonation of which could also make DPF3b less permeable to proton and charge transfer. Although little difference is observed between pH 6 and 8, this is consistent with DPF3b pI in its folded state (6.09) close to pH 6. Nonetheless, the overall protein charge changes from −9 at pH 8 to +4 at pH 6, which may be sufficient to alter the optical properties of DPF3b fibrils. Furthermore, subtle changes in lateral chain pKa accompanying the formation of the amyloid core, not described by our DPF3b model, could also be at work. The steady decrease of the autofluorescence emission with pH (Figs. 1A–C) appears to be exacerbated by further gain in positive charge, increasing to +45 and +68 at pH 4 and 2, respectively. Consequently, increased protonation of DPF3b AmylPRs seems to impair REES, ICT, and proton transfer phenomena, hence enhancing vAF-emitting fluorophores at the expense of dbAF and bgAF ones.

3.4. Effect of basic pH on the autofluorescence properties of DPF3b fibrils

Through the alkalinisation of the fibrillated DPF3b, the autofluorescence fingerprints are once more substantially transformed (Figs. 1E–F). The overall emission intensity is reduced and there is no significant intensity difference between pH 10 and 12. Compared to the other pH conditions, two majority bands of maximum λ_{em} appear at around 375 and 425 nm upon excitation at 310 and 340 nm, respectively. The band at 375 nm also presents a shoulder near 420 nm. Giving its less intense and red-shifted associated emission, excitation at 320 seems to act in the transition from the first to the second emission maximum. Indeed, as better illustrated on normalised spectra, such consistent bathochromic shift between the two maxima occurs within a relatively short window of λ_{ex} (Figs. 2E–F). Furthermore, from the second emission maximum, the intensity progressively decreases at higher excitation wavelengths, with a brief pause for pH 10 at 370 and 380 nm of excitation (Fig. 1E). Such decrease goes along with a continuous red-shift against the Kasha's rule up to an excitation of 430 nm, after which a second 'jump' in the emission wavelength happens (Figs. 2E–F). The latter corresponds to a change from a dbAF to a bgAF mode, as the fluorescence is shifted to 508 and 520 nm after excitation at 440 and 450 nm, respectively. The extent of the bathochromic shift is also significantly reduced in the dbAF region (λ_{ex} 380 to 430 nm).

One can appreciate that both emission maxima of DPF3b fibrils are associated to vAF, the first one even existing at the limit of the violet region. Albeit the dominant autofluorescence mode is also shifted to vAF at low pH, the spectral behaviour at pH 10 and 12 can be distinguished on the basis of its λ_{ex}-λ_{em} dependency. In acidic conditions, vAF emissions obey the Kasha's rule, while it is infringed at basic pH. Basified DPF3b fibrils thus display a triple anti-Kasha vAF-dbAF-bgAF regime presenting a vAF prevalence, where emission maxima are localised, as well as dbAF, because some dbAF-emitting populations are as fluorescent as vAF ones. Similarly to acidic pH, the fraction of bgAF fluorophores is characterised by the lowest quantum yield. Overall, every autofluorescence modes identified for fibrillated DPF3b in an alkaline environment are also anti-Vavilov.

As evidenced by the Poisson-Boltzmann electrostatic potential map of DPF3b, the protein becomes more negatively charged at pH 10 and 12 with a total charge of −26 and −80, respectively (Figs. 4 and S4). The electrostatic potential of both N- and C-terminal regions containing AmylPRs (Fig. S6) is impacted by raising pH, which is consistent with their content of polar and positively charged residues. AmylPR-2 and 5 notably denote as to their depletion in negatively charged amino acids (Fig. S7), likely relating to the spectral properties of DPF3b fibrils at basic pH. Breaking of Kasha's rule is facilitated by REES, ICT, as well as proton transfer reactions that can be hindered through changes in amino acid charge state, as highlighted in acidic conditions.

However, Arg residues that are still protonated in the vicinity of deprotonated Lys and/or Cys residues can probably also promote ITC and excited state intramolecular proton transfer (ESIPT), manifested in the form of the observed anti-Kasha behaviour, as well as emission enhancement in the vAF mode. Nevertheless, lower autofluorescence intensities could be attributed to some extent to the partial disruption of H-bond networks between β-sheets and β-strands, resulting in a loss of electron delocalisation. Furthermore, emission on IPF and ITF spectra observed at pH 10 and 12 in the UVA-near-violet region (Figs. S3A and S3E) can be provided by the major autofluorescence observed at λ_{ex} of 310 nm in such pH conditions. In this context, Trp-vAF emission overlapping is more than conceivable, which is supported by the relative abundance of Trp, Lys, and Arg amino acids in AmylPR-2 and 7 (Fig. S7).

3.5. Excitation contributions to the autofluorescence of DPF3b fibrils at pH 8

Contributions to DPF3b fibrils autofluorescence were further investigated by scanning the emission wavelengths from 400 to 500 nm and analysing the resulting excitation spectra. At the corresponding emission maximum (460 nm), three main bands are uncovered at pH 8 (Fig. 3D). The first one, displaying the highest intensity, is located at 232 nm and has been assigned to peptide bond absorption [43,86]. The second excitation band is detected at 285 nm, falling into the absorption region of aromatic residues. The third one, corresponding to the main autofluorescence component, appears at 398–400 nm, which is coherent with the emission data (Fig. 1D). By transitioning from one

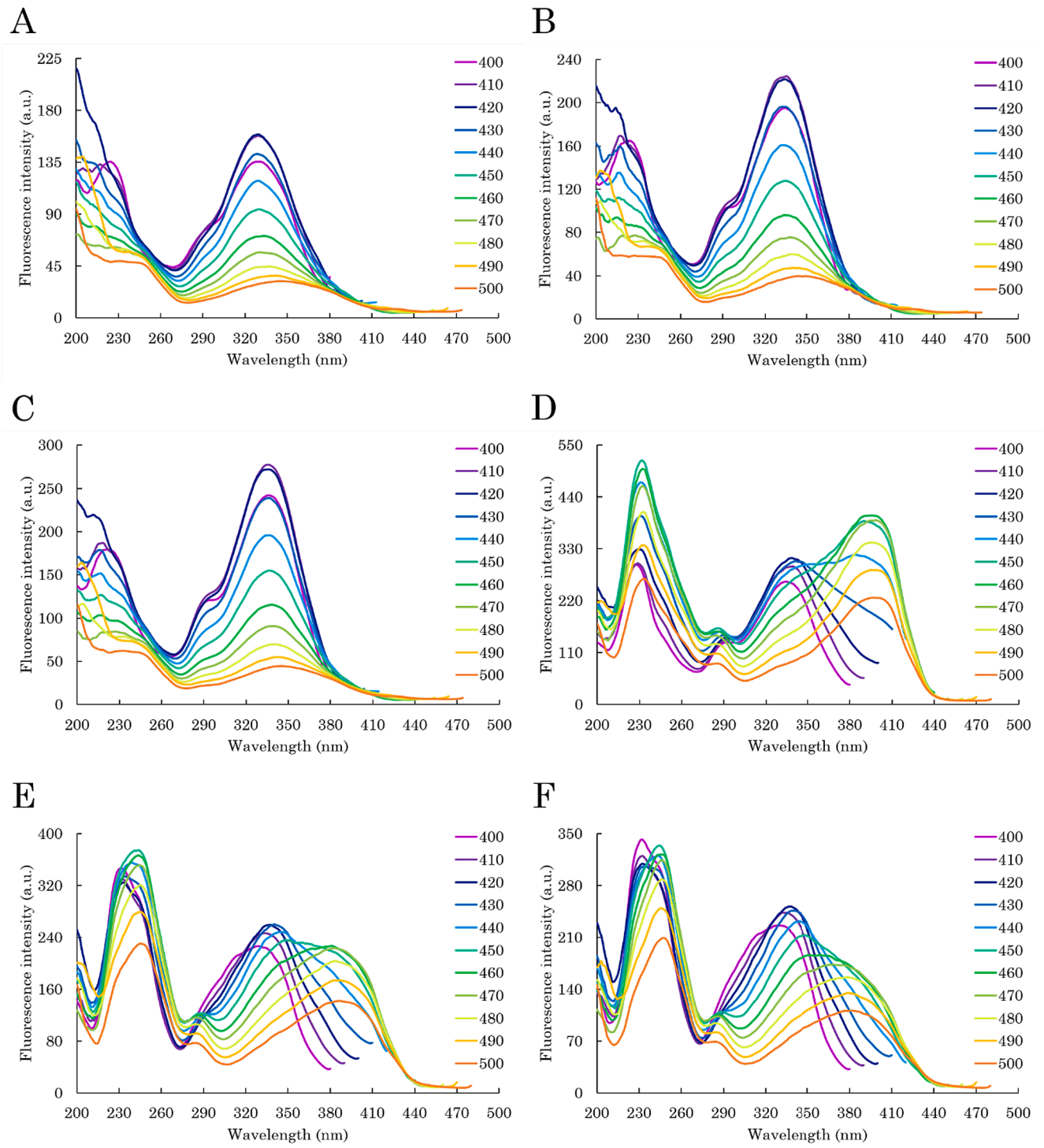

Fig. 3. Autofluorescence excitation spectra of full-length DPF3b amyloid fibrils formed in TBS at ~20 °C (C_{DPF3b} = 5 μM) and adjusted to pH values of (A) 2, (B) 4, (C) 6, (D) 8, (E) 10, and (F) 12 upon emission ranging from 400 to 500 nm (400 ≤ λ_{em} ≤ 500 nm, sw = 10 nm); 400 (magenta), 410 (purple), 420 (dark blue), 430 (blue), 440 (light blue), 450 (turquoise), 460 (green), 470 (khaki), 480 (lime), 490 (ochre), and 500 nm (orange).

autofluorescence mode to another, excitation spectra undergo substantial modifications. In the vAF region, fixing the emission at 400 nm, the λ_{ex} of the peptide bond is slightly blue-shifted to 228 nm with respect to the emission maximum, and its intensity is decreased. While the band associated to aromatic residues is red-shifted to 293 nm, indicating that vAF fluorophores more selectively excite Trp amino acids, that of autofluorescence is blue-shifted towards 334 nm, confirming that vAF emission requires higher activation energy.

As we enter the dbAF range, the most remarkable feature is the emergence of a second autofluorescence band at 384 nm, which rapidly becomes the dominating one up to λ_{em} of 470 nm. What remains of the vAF excitation component manifests in the form of a spectral shoulder at higher emission wavelengths. Such transformation comes with the further enhancement of the peptide absorption, as well as the hypsochromic shift of the aromatic band, the latter suggesting a higher contribution of Tyr residues to dbAF.

In addition, absorption of Phe residues in dbAF mode is difficult to discern because of the spread of the peptide band. Nevertheless, band

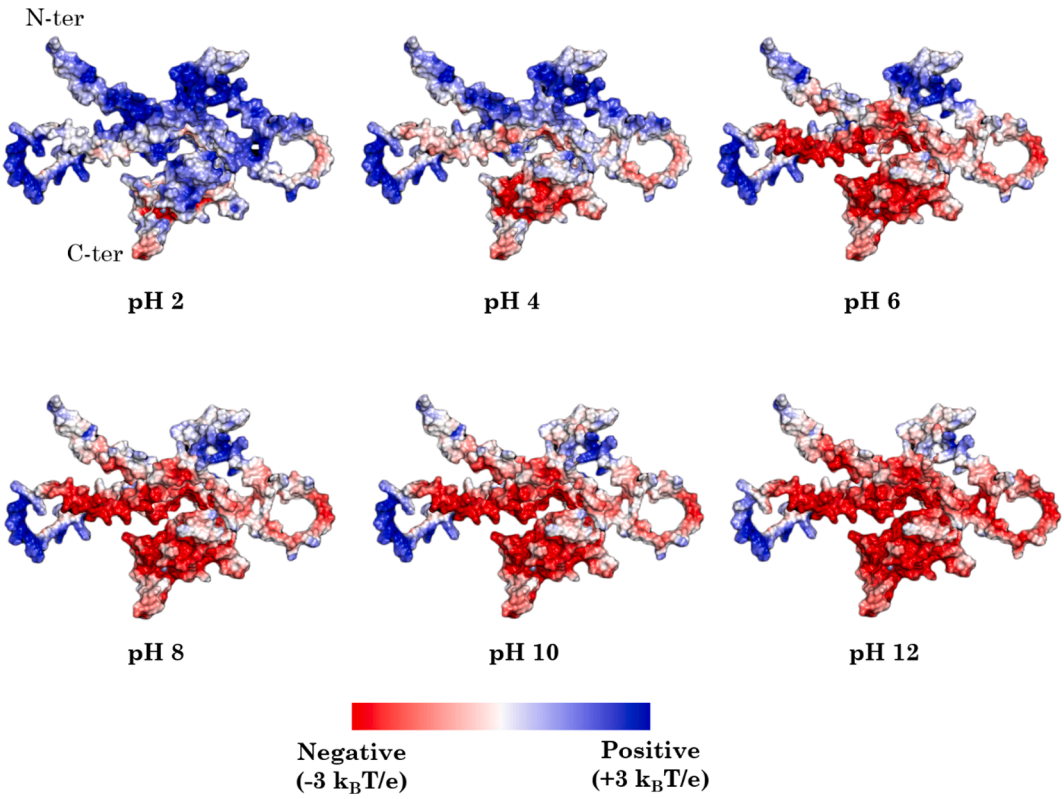

Fig. 4. Mapping of the Poisson-Boltzmann electrostatic potential on the van der Waals surface of full-length DPF3b (MMseqs2-AlphaFold2 model) at pH values of 2, 4, 6 (up row, left to right), 8, 10, and 12 (bottom row, left to right). The electrostatic potential ranges from −3 k_BT/e (red) to +3 k_BT/e (blue). N- and C-termini of the protein are indicated.

bulging near 250–260 nm can be related to the Phe excitation, which is absent at vAF short-wavelength emission. The existence of a dual vAF-dbAF mode, neatly distinguishable on emission spectra (Figs. 1D and 2D), of DPF3b fibrils at pH 8 is corroborated by the signature discrepancies discussed in the section on the excitation spectra (Fig. 3D). On the contrary, lower intensities and absence of spectral shifts at emissions between 480 and 500 nm account for the absence of bgAF, which is completely engulfed by the prevalent dbAF mode.

3.6. Effect of acidic pH on the excitation contributions of DPF3b fibrils autofluorescence

As expected from the emission spectra (Figs. 1A–C), the autofluorescence excitation associated with the vAF emission maximum (415 nm) is shifted to lower wavelength, which is located at around 329 nm at pH 2 and 334–336 nm at pH 4 and 6 (Figs. 3A–C). The excitation value is maintained until λ_{em} of 450 nm, after which the autofluorescence band slowly shifts to the red up to a maximum λ_{ex} of 345–349 nm at the emission at 500 nm. Compared to pH 8, the bathochromic shift appears relatively small with respect to the emission range scanned.

Permanence of more energetic excited states in a short λ_{ex} window is in good agreement with the prevalence of Kasha-obedient vAF mode for acidified fibrils (Figs. 2A–C), as well as the rapid decline of fluorescence intensity beyond 340 nm excitation (Figs. 1A–C). While the position of the autofluorescence band remains essentially unaffected, long-wavelength emission is characterised by a marked decrease of the band intensity, which partially accounts for the weakly dbAF- and bgAF-emitting populations. Furthermore, bgAF minority mode arises from the small spectral humps emerging at long-wavelength excitation from 480 nm of emission.

Interestingly, the peptide bond band is the component that is the most impacted by acidification of DPF3b fibrils. Indeed, while a band is clearly identified at 224 nm by fixing the emission at 400 nm, it becomes more blurred as the emission wavelength is increased. This is particularly true at pH 2, raising the noisiest far-UV signatures. At pH 4 and 6, short-wavelength excitation features are more recognisable with the band position progressively red-shifting from 215 to 217 nm to 236–240 nm by increasing the λ_{em} from 410 nm to 500 nm, along with an intensity decrease. Such changes are arguably involved in the transition from one autofluorescence mode to another, as well as in the observed anti-Vavilov effects.

Regarding the aromatic band, a low absorption between 260 and 280 nm, identifiable by a local spectral depression, explains why autofluorescence is barely detected on IPF and ITyrF spectra in acidic conditions (Figs. S3A and S3C). In such context, engagement of Phe and Tyr residues in autofluorescence is limited. However, the Trp excitation band is detected at 294 nm with an appreciable intensity, especially in vAF emission range, but is gradually extinguished by switching to dbAF and bgAF modes. Conservation of Trp contribution nonetheless correlates with the autofluorescence-mediated bimodal emission on ITF spectra (Fig. S3E).

3.7. Effect of basic pH on the excitation contributions of DPF3b fibrils autofluorescence

At the second emission maximum (425 nm), position of the autofluorescence excitation band at 340 nm (Figs. 3E–F) is in good agreement with the emission spectra (Figs. 1E–F). Such vAF emission is associated with a spectral hump at 295 nm, corresponding to the absorption of Trp residues, as well as to a peptide bond excitation band at 233 nm of high intensity. Further examination of the peptide bond band reveals a shoulder at 245 nm, the intensity of which raises by increasing the λ_{em} from 420 to 450 nm, so much so that it becomes the majority band. Beyond emission at 460 nm, while remaining at 245 nm, the absorption of the peptide bond decreases, following the same trend as the

autofluorescence band.

Such red-shift in the peptide bond band, being all the more perceivable at pH 12 (Fig. 3F), is unique to alkaline conditions, and is really coherent with the continuous anti-Kasha behaviour described for emission spectra (Figs. 2E–F). Consequently, progressive transition from vAF to dbAF (and bgAF) mode is predominantly triggered by the combined and concomitant bathochromic shift of peptide bond and autofluorescence excitation bands, the latter also progressively broadening to the red. Furthermore, their reasonably high intensity over an extended range of λ_{em} also allows for the coexistence of strong-emission vAF and dbAF populations.

The contribution of the intrinsic fluorescence of aromatic residues is mingled with the autofluorescence band at 400 nm of emission, which likely explains the fluorescence enhancement, as well as the band broadening observed on IPF and ITF spectra (Figs. S3A and S3E). The shoulder-like feature of the autofluorescence band on these spectra also

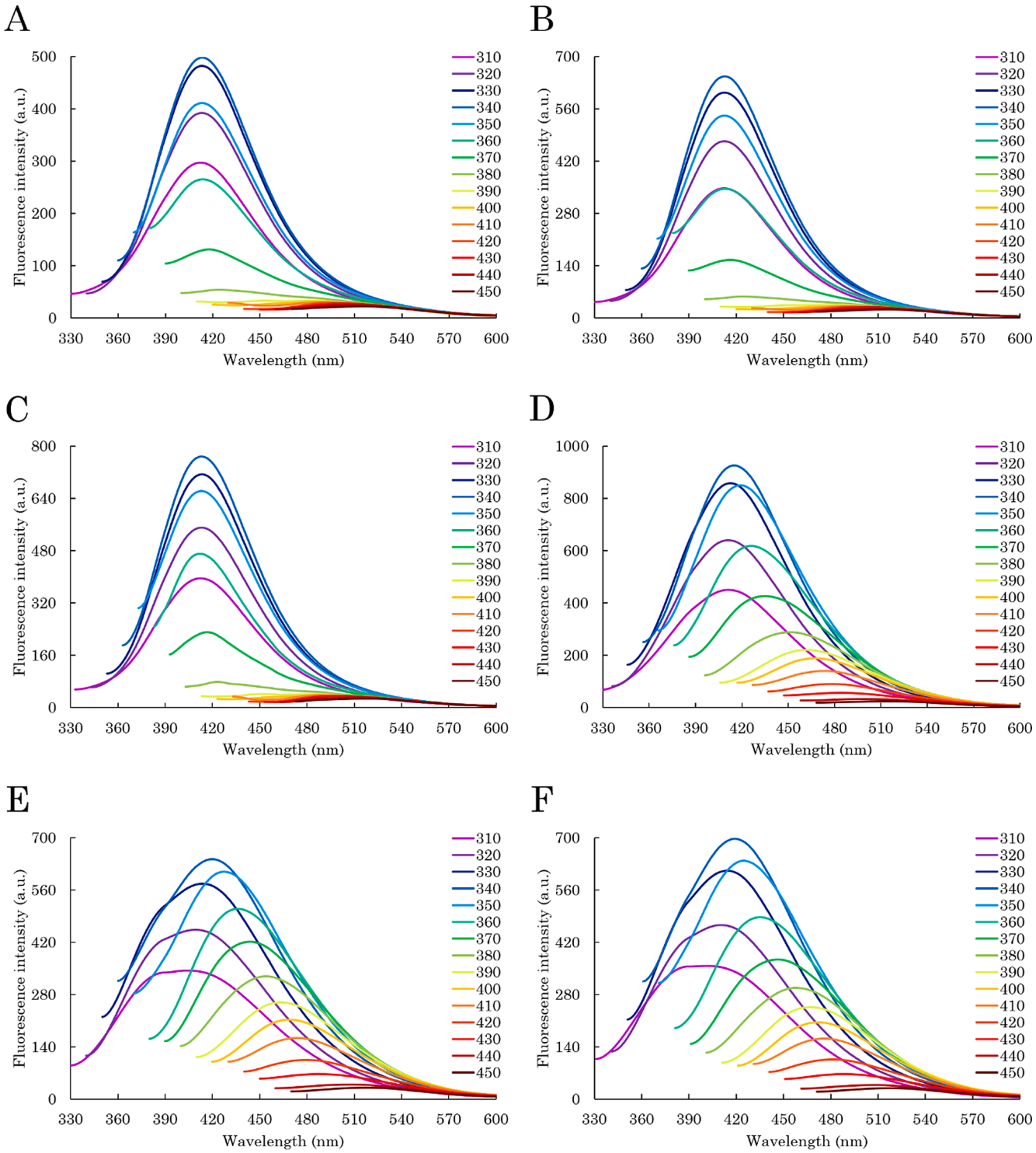

Fig. 5. Autofluorescence emission spectra of full-length DPF3a amyloid fibrils formed in TBS at ~20 °C (C_{DPF3a} = 5 μM) and adjusted to pH values of (A) 2, (B) 4, (C) 6, (D) 8, (E) 10, and (F) 12 upon excitation ranging from 310 to 450 nm (310 ≤ λ_{ex} ≤ 450 nm, sw = 10 nm); 310 (magenta), 320 (purple), 330 (dark blue), 340 (blue), 350 (light blue), 360 (turquoise), 370 (green), 380 (khaki), 390 (lime), 400 (ochre), 410 (orange), 420 (red), 430 (scarlet), 440 (crimson), and 450 nm (merlot).

originates from such aromatic absorption on excitation spectra. In the dbAF-bgAF emission range, the aromatic band is more discernable at 283–285 nm, but decreases in intensity when λ_{em} increases from 460 to 500 nm. Whilst lower absorption intensity is coherent with weaker Tyr contribution compared to pH 8, the hypsochromic shift and reduction of the spectral groove at 275 nm in long-wavelength emission are responsible for the bimodal emission on ITyrF spectra at pH 10 and 12 (Fig. S3C). The same applies to Phe residues, the contribution of which increased in dbAF and bgAF modes with the displacement of the peptide bond band position, accounting for the bathochromic shift of the second emission band observed on IPF spectra (Fig. S3A).

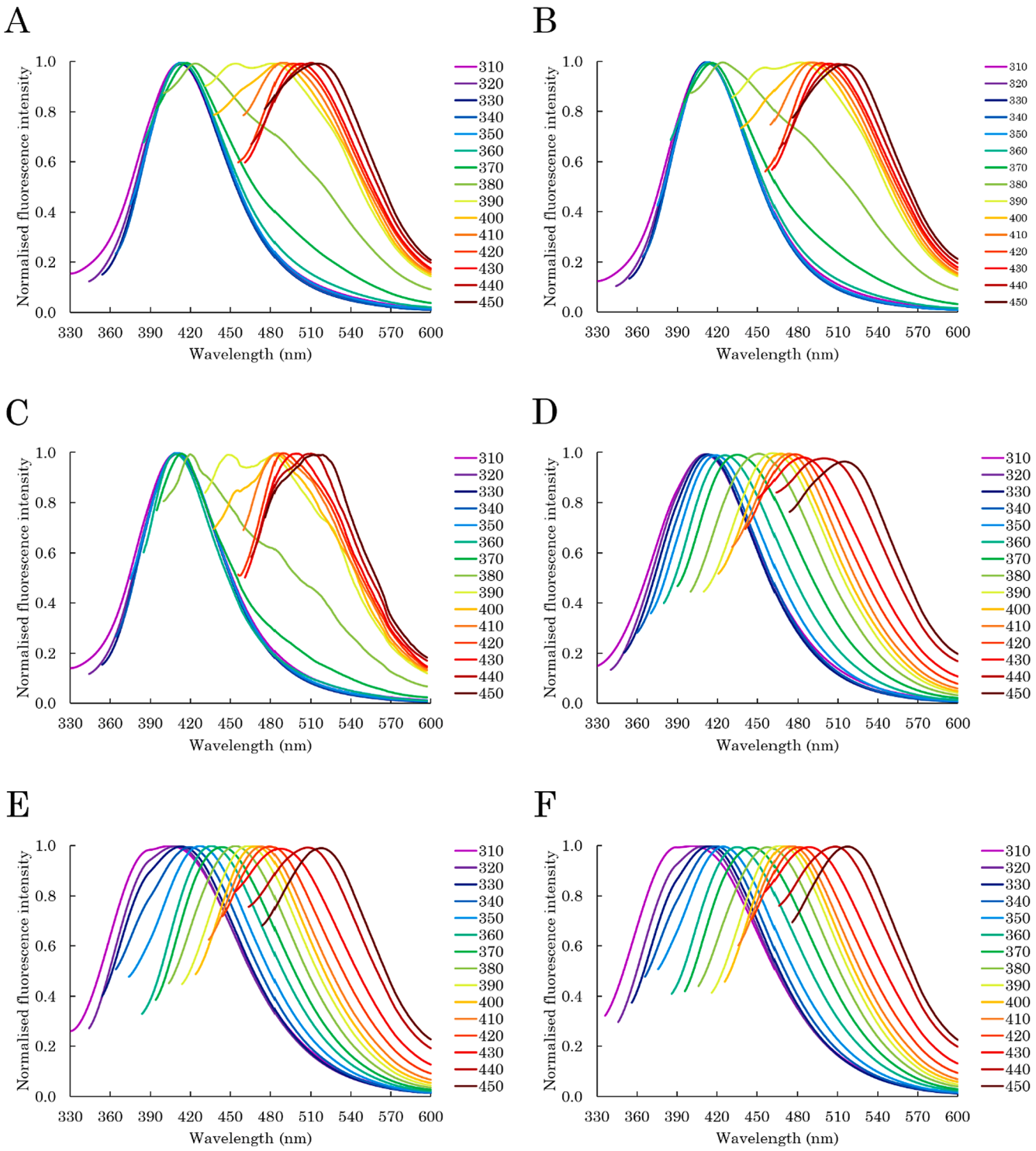

Fig. 6. Normalised autofluorescence emission spectra of full-length DPF3a amyloid fibrils formed in TBS at ~20 °C (C_{DPF3a} = 5 μM) and adjusted to pH values of (A) 2, (B) 4, (C) 6, (D) 8, (E) 10, and (F) 12 upon excitation ranging from 310 to 450 nm (310 ≤ λ_{ex} ≤ 450 nm, sw = 10 nm); 310 (magenta), 320 (purple), 330 (dark blue), 340 (blue), 350 (light blue), 360 (turquoise), 370 (green), 380 (khaki), 390 (lime), 400 (ochre), 410 (orange), 420 (red), 430 (scarlet), 440 (crimson), and 450 nm (merlot).

3.8. Autofluorescence properties of DPF3a fibrils at pH 8

Similarly to DPF3b, the effect of pH on the autofluorescence of DPF3a amyloid fibrils was assessed through the examination of the peculiarities of its emission (Figs. 5–6). At pH 8, the fluorescence intensity rapidly increases from λ_{ex} of 310 nm until it reaches an emission maximum centred at 415 nm after illumination at 340 nm (Fig. 5D). At longer excitation wavelengths (at higher λ_{ex}), the band intensity progressively decreases. As better evidenced in normalised spectra, such intensity variation is accompanied by a relatively gradual and continuous bathochromic shift of the emission band position (Fig. 6D). Indeed, while some Kasha character is conserved between λ_{ex} of 310–330 nm, DPF3a fibrils exhibit a progressively shifting triple vAF-dbAF-bgAF anti-Kasha-Vavilov autofluorescence mode over the selected excitation range. They switch from a dominant vAF (λ_{ex} 310–370 nm) to a weakly fluorescent bgAF mode (λ_{ex} 430–450 nm) via an intermediary dbAF population (λ_{ex} 380–420 nm).

Interestingly, the emission maximum of DPF3a fibrils is more blue-shifted compared to that of DPF3b under the same fibrillation conditions, going squarely from dbAF to vAF. Unlike DPF3b, DPF3a exhibits detectable bgAF emissions in the long-wavelength range. Such differences indicate that the structurally distinct amyloid fluorophores were formed during the course of fibrillation. Furthermore, these specific structural features can explain not only the existence of the bgAF emitters, but also the prevalence of DPF3a vAF at pH 8, accounting for a larger fraction of high-energy fluorophores, in which, nevertheless, ICT, ESIPT, and/or electron delocalisation are to some extent occurring because of the Kasha's rule violation observed at short wavelengths. The overall anti-Kasha behaviour is also indicative of the photoselection of a wide diversity of REES-generated fluorophores.

3.9. Effect of acidic pH on the autofluorescence properties of DPF3a fibrils

Starting from λ_{ex} of 310 nm, the band intensity progressively increases up to a maximum at λ_{em} of 413 and 410 nm (λ_{ex} 340 nm) for pH 2–4 and 6, respectively (Figs. 5A-C). Illumination between 350 and 380 nm results in a steep decrease in the emission intensity, which is followed by a strong extinction of autofluorescence signals in the 390–450 nm λ_{ex} range. Compared to pH 8, short-wavelength excitation leads here to a slightly blue-shifted emission, corresponding to vAF, which does not violate the Kasha's rule over a broader excitation range, from 310 to 360 nm (Figs. 6A-C). Giving the maximum emission, impediment of proton and charge transfer and recombination seems to be very consistent with the formation of vAF populations resistant to REES, similar to the DPF3b fibrils at low pH. Along with the emergence of Kasha-obedient vAF emitters, one can appreciate that the overall spectra intensity is decreased at further acidification of the DPF3a fibrils.

Such fluorescence extinction is likely associated with the protonation-driven quenching of autofluorescence fluorophores also due to the hindering of REES, ICT, ESIPT, and electron delocalisation phenomena. Indeed, AmylPRs of DPF3a are particularly enriched in charged residues (Fig. S8) and localise in the protein regions, for which the computed Poisson-Boltzmann electrostatic potential shows the greatest variability with pH, namely towards the N- and C-termini (Figs. 8 and S5). From pH 6, there is an outright gain in positive charge, rising from −6 (at pH 8) to +6, which is consistent with the calculated pI of DPF3a in both its folded (6.58) and unfolded state (6.73). Further acidification to pH 4 and pH 2 leads to a substantial total charge increase to +48 and +72, respectively, exemplified by local and global enrichment in positive charge on the Poisson-Boltzmann potential surface. Given their relative contents of the Asp and/or Glu residues, as well as their positions in the DPF3a sequence, AmylPR-1, 3, 4, and 6 might therefore be involved in the formation of the photoselected fluorophores, the further protonation of which results in the described autofluorescence alterations. The same could be applied to the highly negatively charged APR-1, 2, and 7, if they were to be found in the fluorescent core.

Strikingly, excitation at 390 nm leads to the broad emission band overlapping the dbAF and bgAF regions (Figs. 6A-C). It seems to serve as a switching point between autofluorescence modes of DPF3a, which is especially true at pH 2 and 4, as this is the only occurrence of dbAF emission over the scanned excitation wavelengths. This short-windowed vAF-to-bgAF transition manifests even more at pH 6, with a discernable double emission band presenting two maxima at λ_{em} of 449 (dbAF) and 482 nm (bgAF), respectively (Fig. 6C).

With respect to the bgAF fluorophores observed at acidic pH, they all display an anti-Kasha-Vavilov spectral behaviour regardless of the pH value. Their associated quantum yield is also significantly lowered compared to pH 8, thus remaining the weakest-emitting population. In that sense, it appears that REES-resilient vAF emitters are favoured upon acidification, resulting in the abrogation of dbAF and reduction of bgAF mode intensity. Consequently, the optical signatures of DPF3a fibrils mediated by acidic pH present a dual vAF-bgAF mode characterised by a short bimodal dbAF-bgAF transition of weak emission. While acidified DPF3b fibrils also display a major vAF mode (Figs. 1A-C), they are differentiated from DPF3a by the coexistence of several dbAF populations (Figs. 2A-C).

3.10. Effect of basic pH on the autofluorescence properties of DPF3a fibrils

Interestingly, alkalinisation of DPF3a fibrils leads to the less distinctive spectral transformations than those of DPF3b (Figs. 5E-F). Emission intensity progressively increases by illuminating from 310 to 340 nm up to an emission maximum centred at 420 nm (λ_{ex} of 340 nm). Beyond such maximum, the fluorescence intensity progressively decreases with the excitation wavelength. In that sense, the overall trend, being similar to that of pH 8, reveals that, compared to DPF3b, DPF3a fibrils present some resistance towards alkaline conditions due to the less base-sensitive structural features. Nevertheless, an overall decrease in autofluorescence emission is observed on the spectra, irrespectively to the alkaline pH. Such quantum yield reduction likely arises from charge state modification, as well as some disruption of H-bond network within DPF3a β-sheeted fibrils, thus partially impairing ICT, ESIPT, and/or π-electron delocalisation. This tendency is better exemplified by the relative abundance and distribution of positively charged amino acids in DPF3a APRs and AmylPRs (Figs. S6 and S8), as well as by the Poisson-Boltzmann electrostatic potential maps (Figs. 8 and S5), showing a noticeable gain in negative charged residues for an overall protein charge of −26 and −84 at pH 10 and 12, respectively.

Additionally, another difference compared to the initial growing conditions is observed at short-wavelength excitation. Whilst Kasha-obedient vAF populations were obtained at pH 8 after excitation in the 310–330 nm range (Fig. 5D), basified DPF3a fibrils straightforwardly display a continuous anti-Kasha behaviour (Figs. 6E-F), suggesting the formation of new REES-permissive vAF fluorophores through water-protein interactions and/or charge or proton transfer. Arg residues with still available protons in the vicinity of negatively charged amino acids (Asp, Glu, and Cys) and Lys in DPF3a APRs/AmylPRs (Fig. S6) could be the driving force of these more energetic anti-Kasha populations. The same tendency was also shown for the DPF3b fibrils in alkaline medium.

Furthermore, the shoulder at short-wavelength excitation becomes more apparent near 380–390 nm (Figs. 5E-F), which is coherent with the band broadening observed on DPF3a IPF and ITF spectra under the same conditions (Figs. S3B and S3F). Trp-vAF emission presumably occurs due to the spectral overlapping, as it is abolished at longer λ_{ex}, and further supports the involvement of AmylPR-2 and 4, as well as APR-7 in the DPF3a amyloid core given their closeness in the content of the Phe and Trp residues (Figs. S6 and S8). Although leading to comparable effects, such Trp-vAF fluorescence is dominant in DPF3b, which is not the case

for DPF3a. This difference could originate from the compositionally different APRs/AmylPRs and amyloid cores of the two DPF3 isoforms. Indeed, DPF3a is more depleted in Trp residues than DPF3b, which respectively contain two and five of them. DPF3b-associated AmylPRs are also more enriched in aromatic amino acids, suggesting a greater implication of Trp and Phe residues sensitive to alkalinisation in amyloid autofluorescence, which consequently leads to the more prominent contribution detected for basified DPF3b fibrils at 375 nm.

In a nutshell, by submitting DPF3a fibrils to basic pH, they exhibit a triple anti-Kasha-Vavilov vAF-dbAF-bgAF mode, with the emission maximum located at 420 nm after excitation at 340 nm. Populations emitting in the vAF region are favoured, REES-permissive, and partially overlap with Trp-Phe fluorescence at short λ_{ex}. Whereas the quantum yield of dbAF fluorophores is slightly enhanced with appreciable spectra intensities, bgAF emitters remain the weakest in the long-wavelength range.

3.11. *Excitation contributions to the autofluorescence of DPF3a fibrils at pH 8*

Excitation spectra of DPF3a fibrils were also recorded at emission wavelengths varying from 400 to 500 nm (Fig. 7). At the initial

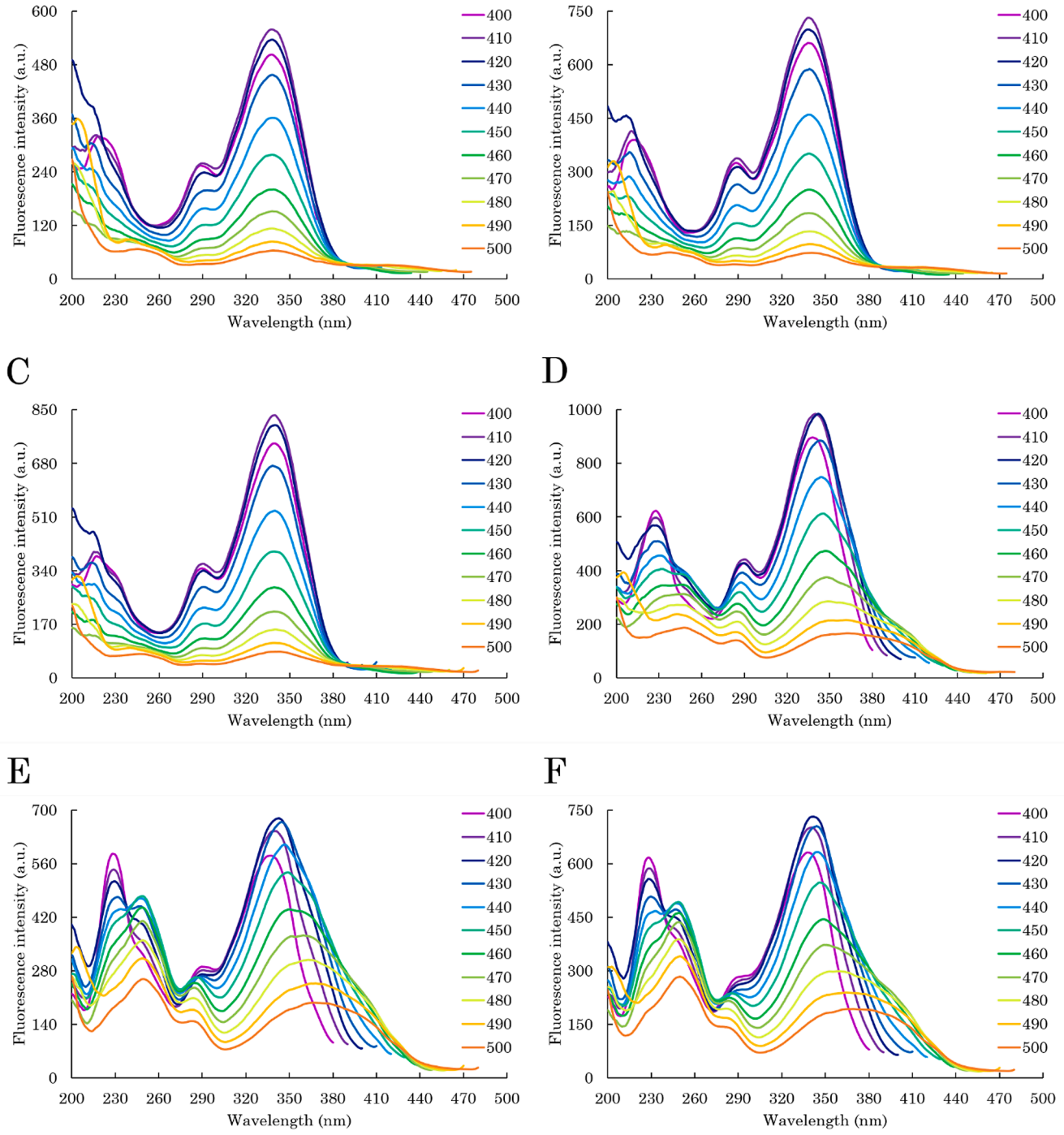

Fig. 7. Autofluorescence excitation spectra of full-length DPF3a amyloid fibrils formed in TBS at ~20 °C (C_{DPF3a} = 5 μM) and adjusted to pH values of (A) 2, (B) 4, (C) 6, (D) 8, (E) 10, and (F) 12 upon emission ranging from 400 to 500 nm (400 ≤ λ_{em} ≤ 500 nm, sw = 10 nm); 400 (magenta), 410 (purple), 420 (dark blue), 430 (blue), 440 (light blue), 450 (turquoise), 460 (green), 470 (khaki), 480 (lime), 490 (ochre), and 500 nm (orange).

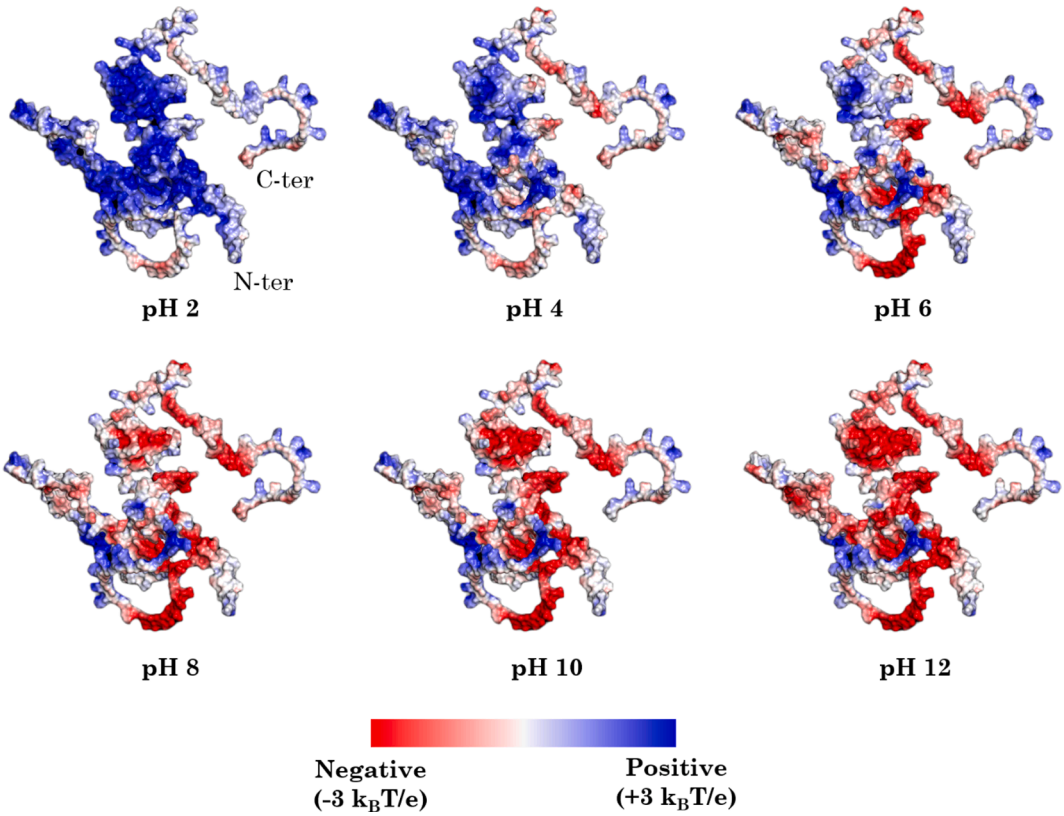

Fig. 8. Mapping of the Poisson-Boltzmann electrostatic potential on the van der Waals surface of full-length DPF3a (MMseqs2-AlphaFold2 model) at pH values of 2, 4, 6 (up row, left to right), 8, 10, and 12 (bottom row, left to right). The electrostatic potential ranges from -3 k_BT/e (red) to $+3$ k_BT/e (blue). N- and C-termini of the protein are indicated.

conditions, the major spectral component, corresponding to the amyloid-related fluorescence, localises at 340 nm for a λ_{em} of 410–420 nm (Fig. 7D), consistent with the emission scans (Fig. 5D). On the same spectra, three other excitation bands can be seen. Two of them, found in the UVC region (200–280 nm) at 227 and 245 nm, are associated with the absorption of the peptide bond. The third band appears at 290 nm and is assigned to the excitation of aromatic amino acids, particularly Tyr and Trp. Existence of a bimodal peptide absorption could be indicative of geometrically peculiar amide bonds forming over the course of DPF3a fibrillation and persisting within its aggregated structure [26].

Switching from one autofluorescence mode to another is accompanied by subtle changes in the obtained signatures. Transition from vAF to dbAF results in the decrease of the band at 227 nm, the increase of the second UVC band, red-shifting to 248 nm, as well as in the emergence of a shoulder near 410 nm of λ_{ex}. In addition, the autofluorescence excitation band gradually red-shifts to 350 nm and decreases in intensity. Whilst the absorption at the aromatic band happens to be also reduced, on the contrary, it undergoes a hypsochromic shift to 285 nm. By emitting to higher wavelengths, up to bgAF, the second peptide-related contribution and the autofluorescence shoulder towards 410 nm become concomitantly more pronounced at the expense of the first peptide absorption and autofluorescence bands, progressively decreasing. The band intensity of aromatic residues is further decreased, while remaining at 285 nm. In good agreement with emission spectra (Fig. 5D), overall high intensity of excitation spectra accounts for the prevalence of vAF populations.

In addition, it appears that dbAF and bgAF modes are not only sustained by photoselecting new emitters at 410 nm, but they also favour Tyr excitation over Trp, which is coherent with the position of the autofluorescence band on DPF3a ITyrF spectrum at pH 8 (Fig. S3D). Although the bathochromic shift of the peptide absorption band also participates in the transition from vAF to dbAF and bgAF, its lower intensity is notably responsible for the limited emission of the two latter modes, which is especially true for bgAF fluorophores. The same applies to the other aromatic and autofluorescence contributions, yielding weakly intense excitation bands in the long-wavelength emission range. Continuous variations in band position and intensity are also coherent with the anti-Kasha-Vavilov behaviour on emission spectra (Fig. 5D).

3.12. Effect of acidic pH on the excitation contributions of DPF3a fibrils autofluorescence

As for the acidified DPF3b fibrils (Figs. 3A-C), excitation spectra are mostly impacted at the level of the peptide bond and autofluorescence contributions (Figs. 7A-C). Whereas the peptide bond band is blue-shifted towards 212–217 nm between 400 and 470 nm of emission, it decreases in intensity and becomes less and less discernable as the emission wavelength increases. Such hypsochromic shift likely originates from the protonation-driven disruption of the amide bond geometry, and participates in the enhancing of Kasha-obedient vAF mode (Figs. 5A-C and 6A-C). It can be pointed out that, over the same range of λ_{em}, a small excitation shoulder is visible at approximately 233 nm at pH 6, which may be one of the reasons why the bimodal dbAF-bgAF transition is more clearly defined on the associated emission spectra (Fig. 6C). Furthermore, bgAF emissions (λ_{em} 480–500 nm) manifest through the steady bathochromic shift of the peptide bond band up to 250 nm.

As expected from the extension of emissions obeying the Kasha's rule, the main autofluorescence contribution is not characterised by any significant shift in band position over the range of scanned λ_{em} (400–500 nm) and is maintained between 338 and 340 nm at pH 2, 4, and 6, showing that protonation causes persistence of more energetic excited states predominantly associated to vAF emission. The steep decrease observed in emission intensity past 340 nm of excitation, as

well as the absence of the defined dbAF mode in acidified DPF3a fibrils can be explained by such conservative behaviour of a vAF-related excitation band position over an extensive range of λ_{em}. On the other hand, the apparition of bgAF populations, observed from λ_{ex} of 390 nm on emission spectra, is most notably a corollary of the tenuous second autofluorescence contribution at 415–420 nm, exclusively occurring in the long-wavelength emission range. Along with the changes in the peptide bond absorption, such spectral hump is responsible for the short-windowed vAF-to-bgAF transition (Figs. 6A-C).

With respect to the absorption band of aromatic residues, it presents a hypochromic effect and a slight bathochromic shift from 289 to 293 nm the higher the emission wavelength, indicating that weakly emitting dbAF and bgAF fluorophores more selectively excite Trp residues. Nonetheless, Trp also participates prevalently in vAF emission, as evidenced in both excitation (Figs. 7A-C) and ITF spectra (Fig. S3F). Higher Trp contribution compared to Phe and Tyr residues is further supported by the large spectral groove observed between 260 and 280 nm, corroborating the overall extinction of the vAF band on IPF and ITyrF spectra at acidic pH (Figs. S3B and S3D). Coherently with emission spectra (Figs. 5A-C), the lower the pH, the weaker the excitation signals. Overall decrease in fluorescence intensity beyond the emission maximum mainly accounts for the observed anti-Vavilov effect on emission spectra.

3.13. Effect of basic pH on the excitation contributions of DPF3a fibrils autofluorescence

At the emission maximum (420 nm), the excitation spectra of basified DPF3a fibrils exhibit four bands (Figs. 7E-F) the positions of which are comparable to that at pH 8 (Fig. 7D). The band of the peptide bond possesses a maximal intensity at 230 nm, as well as a noticeable shoulder at 248 nm. The aromatic band is located at 290 nm, whereas the autofluorescence one reaches its maximum at a λ_{ex} of 343 nm, which correlates well with the emission data (Figs. 5E-F). At lower λ_{em} in the vAF region, the shoulder is reduced in favour of the first peptide bond contribution, and the intensity of the autofluorescence band is decreased; with the exception of the aromatic band, all the contributions are also slightly blue-shifted. This appears to be coherent with the formation of more energetic fluorophores at short-wavelength excitation-emission, which is characteristic of the vAF emitters.

Starting from the emission maximum, increase in λ_{em} results in a gradual bathochromic shift of the peptide bond and autofluorescence excitation bands. Remarkably, transition from vAF to dbAF mode at 440 nm is triggered by the switch in the majority peptide bond contribution, that is, from 230 to 248 nm. Compared to pH 8, alkalinisation enhances the second peptide bond contribution in long-wavelength emission, which is presumably due to changes in the amide group geometry of dbAF and bgAF fluorophores. Regarding autofluorescence, its associated band undergoes a red-shift up to 366 nm along with a steady spectral broadening to higher excitation wavelengths, as well as an intensity decrease. In contrast to acidic conditions, such base-mediated band shift and broadening towards the long-wavelength excitation range reflects the coexistence of the dbAF and bgAF modes of appreciable intensity with the vAF mode in emission spectra (Figs. 5E-F). This mechanism is concomitantly promoted by the switch in peptide bond absorption.

The absorption of aromatic residues of fibrillated DPF3a is also subject to modifications at pH 10 and 12. By progressing from vAF to dbAF and bgAF, the aromatic band is blue-shifted from 290 to 282 nm. Interestingly, the same tendency was observed for basified DPF3b fibrils and is indicative of a higher contribution of Tyr over Trp residues. Furthermore, reduction of the spectral depression at 270–275 nm enhances Tyr-promoted dbAF, hence manifesting as the red-shifted bimodal emission on ITyrF spectra in basic conditions (Fig. S3D). Such optical behaviour has also been detected in IPF spectra (Fig. S3B), which particularly arises from the increased Phe involvement in dbAF and bgAF emissions due to the bathochromic shift of the peptide bond band. Therefore, the continuous violation of Kasha's rule described in emission spectra (Figs. 6E-F) finds its origin in such changes in the peptide, aromatic, and autofluorescence components, while fluctuations in the fluorescence intensity amongst the various excitation bands account for the anti-Vavilov effect.

Amide bond deformation, as well as change in its geometry and communication have been proposed as an influencing factor of protein and peptide aggregate autofluorescence [26]. Therefore, spectral transformations occurring in the far-UV range on excitation spectra, in other words alteration of the peptide bond absorption, are in all likelihood an indicator of the peptide/amide bond geometrical distortions, induced here by modification of the hydrogen bond network due to pH. Such variations possess a non-negligible impact on the mode and quantum yield of autofluorescence populations, as evidenced on excitation spectra of DPF3b fibrils in diverse pH conditions (Fig. 3), hence helping to some extent to the overall intensity decrease of autofluorescence excitation, as well as to the shift in autofluorescence mode.

In the case of DPF3a fibrils, the importance of the far-UV range absorption of the peptide bond is emphasised once again by the definition of their optical properties (Fig. 7). (De)protonation-driven perturbation of the amide bond geometry along with photoselection of aromatic residues are determinant for the mode and quantum yield of autofluorescence. Strikingly, DPF3a excitation spectra unveil that, regardless of the pH condition, the autofluorescence band at the emission maximum remains the dominant contribution with respect to the peptide bond absorption, which was not the case of DPF3b fibrils. Such discrepancy in spectral response is informative about the components establishing the optical activity of DPF3 fibrils, as well as isoform-specific structural features in their respective amyloid core.

3.14. Contribution of room temperature phosphorescence to DPF3b and DPF3a fibrils autofluorescence

Along with its unique fluorescence properties, Trp amino acid has also been reported to emit persistent luminescence in the visible range, which is remarkably measurable even in the dissolved liquid phase at room temperature [87]. Such phenomenon is commonly referred to as room temperature phosphorescence (RTP) and manifests in proteins after illumination with both UVB and UVA, as well as with blue light from the micro- to the second timescale [88]. Therefore, RTP of Trp in the UVB (λ_{ex} of 295 nm) and longer wavelength excitation range (λ_{ex} of 400 and 450 nm) has been investigated to determine if their intrinsic phosphorescence can to some extent account for the autofluorescence signatures, especially bgAF emission, which have been described and detailed so far.

In each tested pH condition and regardless of the autofluorescence mode, DPF3b and DPF3a amyloid fibrils both exhibit very short-lived Trp RTP (Figs. S9 and S10), with lifetimes in the (sub)microsecond range (Table S1), which relates to very weak phosphorescence emission. Such lifetime shortening is due to the rapid depopulation of the triplet excited state through nonradiative relaxation and quenching effects. Trp RTP is notably known to be significantly quenched by oxygen in air-exposed water concentration and several amino acid side chains, such as Cys, Tyr, and His. In addition, long-lived Trp RTP has been shown to correlate with the burial state of Trp residues in proteins [89,90].

Therefore, it is most likely that the strong extinction of Trp RTP observed for DPF3b and DPF3a fibrils is not only induced by the partial exposure of their Trp residues to the air-oxygenated solvent, as evidenced by ITF spectra (Figs. S3E and S3F), but also by Cys, Tyr, and/or His amino acids proximal to Trp residues in their primary structure (Fig. S6). Although detected, RTP associated to Trp and long-wavelength excitation thus do not contribute to DPF3 amyloid autofluorescence, and more particularly to the emergence of weak bgAF emitters, because of the very short RTP lifetime and intensity.

3.15. pH-dependent autofluorescence red edge shift plots of DPF3b and DPF3a fibrils

In-depth description of the optical properties of the two fibrillated DPF3 isoforms in the UV–visible range, as well as their response to pH variation has allowed to refine the autofluorescence nomenclature into different modes and to highlight REES-mediated anti-Kasha behaviours. Deeper understanding of such unique spectral signatures can be achieved through the construction of red edge shift plots, consisting in the evolution of the maximum autofluorescence emission wavelength, determined from the emission data (Figs. 1, 2, 5, and 6) as a function of the excitation wavelength (Fig. 9).

Red edge shift trends are visually evocative between isoforms and further exemplify how they differently react spectroscopically to changes in the medium conditions. At the initial aggregating conditions, DPF3b amyloid fibrils display a discontinuous dual vAF-dbAF autofluorescence mode (Fig. 9A). Albeit some blue-green emission was recorded at long-wavelength excitation, its very weak and noisy signal proved insufficient to discriminate a true bgAF population (Figs. 1D and 2D). The aforementioned discontinuity is marked by the existence of two plateaux, the first one in the vAF region at short-wavelength excitation, the other over a more extended λ_{ex} range during dbAF emission. Such plateaux are indicative of the photoselection of emitters obeying the Kasha's law over a defined excitation range, which particularly characterises most of the dbAF fluorophores.

In comparison, DPF3a fibrils at pH 8 harbour a discontinuous triple vAF-dbAF-bgAF autofluorescence mode, presenting a single and short Kasha plateau at short-wavelength excitation in vAF (Fig. 9B). Apart from displaying a proper bgAF mode in the long-wavelength excitation, they further differentiate themselves from DPF3b aggregates by their entirely anti-Kasha dbAF population. DPF3a is also characterised by the photoselection of vAF fluorophores over a wider range of excitation wavelengths compared to DPF3b.

At acidic pH, DPF3b exhibits a discontinuous triple vAF-dbAF-bgAF autofluorescence mode with a single but longer plateau obeying the Kasha's rule at the low-wavelength excitation in the vAF region (Fig. 9A). While the extent of REES is significantly reduced for vAF emitters, it is on the contrary enhanced over the course of the vAF-to-dbAF transition, as well as in the dbAF mode, the evolution of which is almost linear. Such REES promotion subsequently results in the generation of bgAF populations with the long-wavelength excitation, which was not observed at pH 8 due to the dominance of the dbAF fluorophores obeying the Kasha's rule.

Interestingly, a comparable tendency is unveiled on the red edge shift plots of DPF3a in acidic conditions (Fig. 9B). Obedience of Kasha's law is indeed extended to longer excitation wavelengths in vAF mode due to the protonation-mediated impairment of REES, charge and/or proton transfer. This reveals that acidification promotes the formation of the optically similar vAF fluorophores between isoforms, which are not only found at the same emission values, but they are also much alike in terms of Kasha-obeying behaviour. However, at longer excitation wavelengths, the fluorescence response noticeably differs. Whilst transition from dbAF to bgAF mode adopted some linearity for DPF3b, acidic conditions not only abrogate the formation of dbAF emitters, but also generate vAF and bgAF modes that are well separated. Whereas REES could be at play, photoselection of two distinct optically active populations seems more probable. In that sense, protonation of DPF3a appears more restrictive in terms of fluorophore modulation, as well as more efficient in REES suppression thanks to a compositionally different amyloid core.

Upon alkalinisation, the red edge shift trends undergo less pronounced transformations for the two isoforms. In both cases, they display an overall anti-Kasha triple vAF-dbAF-bgAF autofluorescence mode, the evolution of which is relatively close to pH 8. Lower emission maxima (λ_{ex} of 310–320 nm) at the limit of the violet spectral range originate from Trp-vAF overlapping fluorescence. Furthermore, dbAF fluorophores deviate from Kasha's rule the more basic the pH, hence allowing the formation of a detectable bgAF mode. REES is also promoted for DPF3a at pH 10 and 12, as evidenced by the dotted curves slightly shifted to longer λ_{em} (Fig. 9B).

Once more, such autofluorescence fingerprints are particularly revealing about the fibril identity of each DPF3 isoform. Although the discrepancy in emission values and fluorophores populating each active autofluorescence mode is remarkable because of the structurally and/or compositionally distinct amyloid cores, comparable REES enhancement most likely arises from the similar alkalinisation-mediated effects due to the conservation of amino acids presenting identical physico-chemical properties in the fibrillar assembly. The same reasoning can be applied to the acid-generated vAF fluorophores of DPF3b and DPF3a aggregates.

Complementarily, the autofluorescence excitation band can be extracted from the excitation spectra (Figs. 3 and 7) with respect to the scanned emission wavelength in order to better appreciate their photoselectivity, as well as REES permittivity. These excitation red edge shift plots, corresponding to the evolution of the maximum

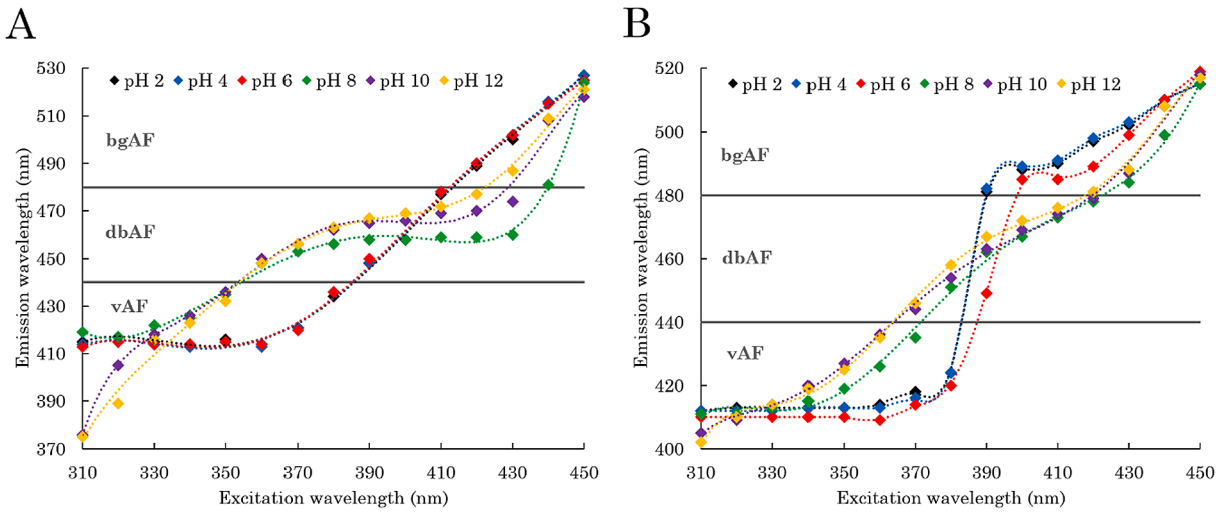

Fig. 9. Red edge shift plot of the maximum autofluorescence emission wavelength ($\lambda_{em,\ max}$) as a function of the excitation wavelength (λ_{ex}) of full-length (A) DPF3b and (B) DPF3a amyloid fibrils formed in TBS at ~20 °C (C_{DPF3} = 5 μM) and adjusted to pH values of 2 (black), 4 (blue), 6 (red), 8 (green), 10 (purple), and 12 (yellow). Red edge shift trends are represented as dotted lines in the pH-associated colour. On each plot, the range of identified autofluorescence modes (vAF, dbAF, and bgAF) is delineated by a gray solid line.

autofluorescence-related excitation wavelength as a function of the autofluorescence emission wavelength, also reveal evocative pH dependency and isoform specificity (Fig. 10). At the initial growing conditions, the excitation wavelength of DPF3b fibrils remains relatively constant in the vAF region before consequently increasing upon switching to dbAF (Fig. 10A). Throughout dbAF and bgAF modes, less variation is observed, and the excitation position appears rather steady. Regarding DPF3a at pH 8, the vAF-to-dbAF transition is contrarily characterised by a progressive increase in the maximum λ_{ex}, the leap of which only occurs by entering the bgAF region (Fig. 10B). Such tendencies further advocate for the emergence of distinct autofluorescence emitters from structurally different isoform-specific fibrils.

For the two fibrillated isoforms, lowering the pH results in a substantial decrease of their excitation maximum, as well as in hindering of the excitation red-shift. Considering DPF3b, the excitation maximum position is not displaced in vAF mode, whereas it slightly and gradually increases during the transition to the dbAF and bgAF regions. Such λ_{ex} restriction is even more extensive for acidified DPF3a fibrils, the excitation maximum of which remains overall constant irrespectively to the selected autofluorescence emitter. In that respect, the suppression effect of the DPF3a acidification on REES is really consistent with the imperturbability of the excitation maximum throughout all the emission scan, supporting that other contributions, such as peptide bond absorption (Figs. 7A-C), are responsible for the change in autofluorescence mode.

Alkalinisation of DPF3b fibrils singularly impacts their excitation red edge shift plots (Fig. 10A). While illumination of vAF emitters occurs according to a progressive increase in the λ_{ex} for the two basic conditions, the profile of the latter diverges within the dbAF region. Indeed, at pH 10, the tendency is much alike to that of pH 8, with an important increase in the excitation maximum, followed by a plateau from dbAF to bgAF transition. Comparatively, the excitation maximum pursues its gradual increase throughout the dbAF range at pH 12 and only reaches an excitation plateau in the bgAF mode. Because these variations are far less reflected in the emission data, they may be partially levelled by other excitation contributions, particularly the major bathochromic shifts noticed for the peptide bond excitation band at both pH 10 and 12 (Figs. 3A-B).

For DPF3a, excitation red edge shift plots at basic pH (Fig. 10B) agree well with the corresponding emission plots (Fig. 9B). Indeed, their trend is fairly similar to that of pH 8, and the anti-Kasha behaviour is coherent with the steady increase in λ_{ex} with a bigger gap towards the dbAF-to-bgAF transition. An overall red-shift of the maximum excitation wavelength is also observed throughout the scanned emission range, ascertaining the REES-enhancer effect of deprotonation on DPF3a fibrils.

4. Conclusions

The two isoforms of the zinc finger protein DPF3, known as DPF3b and DPF3a, have recently been identified as new amyloidogenic IDPs. Amongst their typical amyloid spectroscopic fingerprints, they both exhibit a new intrinsic fluorescence in the visible range over the course of their fibrillation. Such phenomenon is mainly referred to as blue or deep-blue autofluorescence in the literature and has been reported for various (non)-amyloid protein and peptide species. Although several factors have been suggested to alter and contribute to deep-blue autofluorescence, its referential use is still overlooked and the elucidation of its genesis in fibrillar assemblies remains elusive, which is especially true for DPF3. In the present study we sought out therefore to enhance our comprehension of the physico-chemical origins of autofluorescence in DPF3 isoform fibrils, as well as to assess their pH-dependent optical modulation and sensitivity towards a better appreciation of such unique intrinsic fluorescence for the characterisation of amyloid aggregates.

Based on our results, we first and foremost proposed to redefine the nomenclature of the autofluorescence phenomenon by classifying it according to the wavelength ranges of the visible electromagnetic spectrum in which it occurs, as well as by assigning new autofluorescence modes and transitions through a complete description and cross-check of emission and excitation data. Upon illumination in the UV–visible range and in a pH-dependent manner, we have unravelled that fibrillated DPF3 isoforms can either exhibit violet (vAF, λ_{em} 380–440 nm), deep-blue (dbAF, λ_{em} 440–480 nm), or blue-green autofluorescence (bgAF, λ_{em} 480–530 nm). Behaviour within modes could be described as anti-Kasha-Vavilov depending on the existence of fluorescence populations obeying or not the Kasha's and Vavilov's rules. Through spectroscopy characterisation and the use of this new nomenclature, we were able to discriminate the spectral response of DPF3b and DPF3a fibrils towards pH variation, further suggesting that the two mostly aggregate into structurally distinct fibrils.

Discrimination of isoform-specific optical features was deepened by the construction of emission and excitation red edge shift plots. Such representations not only helped to the visualisation of autofluorescence modes and transitions, but also to the highlighting of spectral tendencies

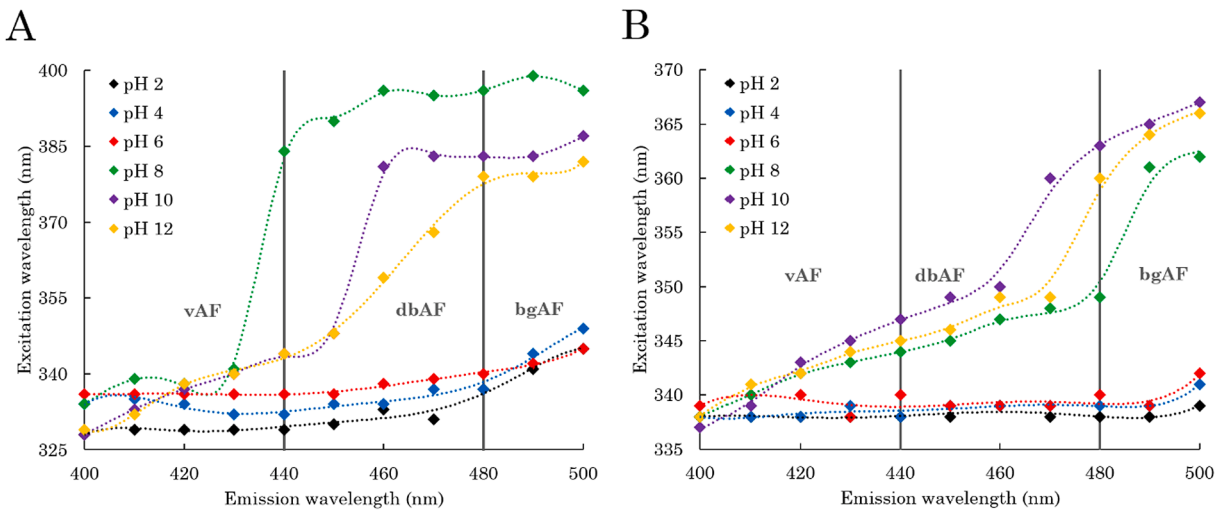

Fig. 10. Red edge shift plot of the maximum autofluorescence-related excitation wavelength ($\lambda_{ex,\ max}$) as a function of the autofluorescence emission wavelength (λ_{em}) of full-length (A) DPF3b and (B) DPF3a amyloid fibrils formed in TBS at ~ 20 °C (C_{DPF3} = 5 μM) and adjusted to pH values of 2 (black), 4 (blue), 6 (red), 8 (green), 10 (purple), and 12 (yellow). Red edge shift trends are represented as dotted lines in the pH-associated colour. On each plot, the range of identified autofluorescence modes (vAF, dbAF, and bgAF) is delineated by a gray solid line.

which are unique to each DPF3 isoform. It allows a more complete description of their autofluorescence populations and a better understanding of their photoselection mechanism. Our results thus advocate for the emergence of distinct autofluorescence emitters from structurally isoform-specific fibrils, which can be photoselectively illuminated thanks to their unique excitation-emission properties.

Throughout this research work and by drawing on the literature, several phenomena were suggested for explaining such pH variations. Anti-Kasha response was mainly attributed to REES arising from the slow dipolar relaxation of water molecules enclosed within the fibril structure, and the extent of which can be reduced through the pH-mediated release of water molecules. Complementarily, REES permittivity and violation of Kasha's rule are likely heavily impacted by ICT, ESIPT, and charge recombination within the amyloid core. Indeed, such electronic mechanisms can be either enhanced or impaired by the (de) protonation of charged and polar amino acids constituting the fibrillar structure, which have been found to be enriched in predicted AmylPRs and APRs of the two DPF3 isoforms.

As remarkably evidenced at the level of the peptide bond absorption band on excitation spectra, deformation of the amide bond geometry and change in its H-bond communication contribute to the observed anti-Vavilov effect and to transition between autofluorescence populations. Disruption of H-bond-aided π-electrons delocalisation through the β-strands and β-sheets interaction network are also much likely to intervene in the (de)stabilisation of ground and excited states, leading to the various pH-dependent Kasha-Vavilov behaviours. Charge transfer from N- to C-termini can also contribute to autofluorescence and should not be excluded in our picture, as it is presumably altered with respect to the pH. Although specific DPF3b and DPF3a autofluorescence-relevant AmylPRs and APRs have been emphasised due to their compositional bias and position with respect to the electrostatic potential maps, their contribution, as well as that of other predicted AmylPRs and/or APRs need to be experimentally verified and explored by carrying out aggregation autofluorescence assays on selected DPF3 segments.

Because amyloid fibrils are highly subject to polymorphism, which is still poorly characterised by spectroscopic meanings, investigation needs to be carried out, notably by assessing the influence of several physico-chemical parameters on the aggregation mechanism of the two DPF3 isoforms. Thus, one can expect the advent of factor-driven morphological diversity, which will also be reflected in the autofluorescence fingerprints. For instance, we have already proved by combining spectroscopic and microscopic techniques that the optical activity of DPF3 fibrils is intimately linked to its amyloid structure, and that divalent metallic cations were capable of altering both in a correlating manner. This question of fibrillar polymorphism could also be further addressed in other better known amyloidogenic proteins by the use of our fluorescence methodology.

In a nutshell, this study showed that fibril optical properties can be modulated through pH variation to reveal (de)protonation-driven modifications of amyloid cores, which may be structurally relevant and informing about the factors that actively participate in such fluorescence. Whilst the photophysics of amyloid aggregates is likely heterogeneous and intricate, there is still much to learn from their intrinsic optics. Therefore, we particularly think that amyloid-related autofluorescence phenomena observed in diverse amyloidogenic protein and peptide systems should be further investigated by the combined and cross-checked analysis of the emission-excitation spectra, autofluorescence modes and transitions, as well as red edge shift plots in selected conditions. Complementarily, time-resolved photoluminescence studies could also prove to be very insightful. This will not only help discriminating distinct fibrillar aggregates based on their optical-structural property relationships, but also deciphering the origins of autofluorescence in such pathologically-significant macromolecular assemblies.

CRediT authorship contribution statement

Julien Mignon: Methodology, Validation, Writing – original draft, Writing – review & editing, Data curation, Conceptualization. **Tanguy Leyder:** Writing – review & editing, Validation, Data curation. **Denis Mottet:** Writing – review & editing, Validation. **Vladimir N. Uversky:** Writing – review & editing, Validation. **Catherine Michaux:** Writing – review & editing, Validation, Supervision, Conceptualization.

Declaration of competing interest

The authors declare that they have no known competing financial interests or personal relationships that could have appeared to influence the work reported in this paper.

Data availability

Data will be made available on request.

Acknowledgements

Authors are grateful to the Research Unit in Biology of Microorganisms (URBM) of the University of Namur. J. Mignon and T. Leyder thank the Belgian National Fund for Scientific Research (F.R.S.-FNRS) for their Fund for Research training in Industry and Agriculture (FRIA) Doctoral grant and Research Fellow fellowship, respectively. D. Mottet and C. Michaux also thank the FNRS for their Senior Research Associate position. This research did not receive any specific grant from funding agencies in the public, commercial, or not-for-profit sectors.

Appendix A. Supplementary data

Supplementary data to this article can be found online at https://doi.org/10.1016/j.saa.2024.124156.

References

[1] C.S. Liang, D.J. Li, F.C. Yang, P.T. Tseng, A.F. Carvalho, B. Stubbs, T. Thompson, C. Mueller, J. Il Shin, J. Radua, R. Stewart, T.K. Rajji, Y.K. Tu, T.Y. Chen, T.C. Yeh, C.K. Tsai, C.L. Yu, C.C. Pan, C.S. Chu, Mortality rates in Alzheimer's disease and non-Alzheimer's dementias: a systematic review and meta-analysis, Lancet Heal, Longev. 2 (2021) 479–488, https://doi.org/10.1016/S2666-7568(21)00140-9.

[2] I.C. Lampropoulos, F. Malli, O. Sinani, K.I. Gourgoulianis, G. Xiromerisiou, Worldwide trends in mortality related to Parkinson's disease in the period of 1994–2019: Analysis of vital registration data from the WHO Mortality Database, Front. Neurol. 13 (2022), https://doi.org/10.3389/fneur.2022.956440.

[3] T.A. Bayer, Proteinopathies, a core concept for understanding and ultimately treating degenerative disorders? Eur. Neuropsychopharmacol. 25 (2015) 713–724, https://doi.org/10.1016/j.euroneuro.2013.03.007.

[4] M.R. Ajmal, Protein Misfolding and Aggregation in Proteinopathies: Causes, Mechanism and Cellular Response, Diseases. 11 (2023), https://doi.org/10.3390/diseases11010030.

[5] M.B. Abubakar, K.O. Sanusi, A. Ugusman, W. Mohamed, H. Kamal, N.H. Ibrahim, C.S. Khoo, J. Kumar, Alzheimer's Disease: An Update and Insights Into Pathophysiology, Front. Aging Neurosci. 14 (2022), https://doi.org/10.3389/fnagi.2022.742408.

[6] P. Calabresi, A. Mechelli, G. Natale, L. Volpicelli-Daley, G. Di Lazzaro, V. Ghiglieri, Alpha-synuclein in Parkinson's disease and other synucleinopathies: from overt neurodegeneration back to early synaptic dysfunction, Cell Death Dis. 14 (2023), https://doi.org/10.1038/s41419-023-05672-9.

[7] A.I.P. Taylor, R.A. Staniforth, General Principles Underpinning Amyloid Structure, Front. Neurosci. 16 (2022), https://doi.org/10.3389/fnins.2022.878869.

[8] J.L. Jiménez, E.J. Nettleton, M. Bouchard, C.V. Robinson, C.M. Dobson, H.R. Saibil, The protofilament structure of insulin amyloid fibrils, Proc. Natl. Acad. Sci. U. S. A. 99 (2002) 9196–9201, https://doi.org/10.1073/pnas.142459399.

[9] H. Wu, S. Movafaghi, I.M. Francino Urdániz, T.M. Rowe, A. Goodwin, T. W. Randolph, Insulin Fibril Formation Caused by Mechanical Shock and Cavitation, J. Phys. Chem. B. 125 (2021) 8021–8027, https://doi.org/10.1021/acs.jpcb.1c01997.

[10] F.G. De Felice, M.N.N. Vieira, M.N.L. Meirelles, L.A. Morozova-Roche, C. M. Dobson, S.T. Ferreira, Formation of amyloid aggregates from human lysozyme and its disease-associated variants using hydrostatic pressure, FASEB J. 18 (2004) 1099–1101, https://doi.org/10.1096/fj.03-1072fje.

[11] R.K. Kar, Z. Gazova, Z. Bednarikova, K.H. Mroue, A. Ghosh, R. Zhang, K. Ulicna, H. C. Siebert, N.E. Nifantiev, A. Bhunia, Evidence for Inhibition of Lysozyme Amyloid

Fibrillization by Peptide Fragments from Human Lysozyme: A Combined Spectroscopy, Microscopy, and Docking Study, Biomacromolecules. 17 (2016) 1998–2009, https://doi.org/10.1021/acs.biomac.6b00165.
[12] J. Juárez, P. Taboada, V. Mosquera, Existence of different structural intermediates on the fibrillation pathway of human serum albumin, Biophys. J. 96 (2009) 2353–2370, https://doi.org/10.1016/j.bpj.2008.12.3901.
[13] M. Maciazek-Jurczyk, K. Janas, J. Pozycka, A. Szkudlarek, W. Rogoz, A. Owczarzy, K. Kulig, Human Serum Albumin Aggregation/Fibrillation and its Abilities to Drugs Binding, Molecules. 25 (2020), https://doi.org/10.3390/molecules25030618.
[14] F.T.S. Chan, G.S. Kaminski, J.R. Kumita, C.W. Bertoncini, C.M. Dobson, C. F. Kaminski, Protein amyloids develop an intrinsic fluorescence signature during aggregation, Analyst. 138 (2013) 2156–2162, https://doi.org/10.1039/c3an36798c.
[15] T.N. Tikhonova, N.R. Rovnyagina, A.Y. Zherebker, N.N. Sluchanko, A.A. Rubekina, A.S. Orekhov, E.N. Nikolaev, V.V. Fadeev, V.N. Uversky, E.A. Shirshin, Dissection of the deep-blue autofluorescence changes accompanying amyloid fibrillation, Arch. Biochem. Biophys. 651 (2018) 13–20, https://doi.org/10.1016/j.abb.2018.05.019.
[16] M. Ziaunys, T. Sneideris, V. Smirnovas, Exploring the potential of deep-blue autofluorescence for monitoring amyloid fibril formation and dissociation, PeerJ. (2019), https://doi.org/10.7717/peerj.7554.
[17] N. Balasco, C. Diaferia, E. Rosa, A. Monti, M. Ruvo, N. Doti, L. Vitagliano, A Comprehensive Analysis of the Intrinsic Visible Fluorescence Emitted by Peptide/Protein Amyloid-like Assemblies, Int. J. Mol. Sci. 24 (2023), https://doi.org/10.3390/ijms24098372.
[18] D. Pinotsi, A.K. Buell, C.M. Dobson, G.S. Kaminski Schierle, C.F. Kaminski, A. Label-Free, Quantitative Assay of Amyloid Fibril Growth Based on Intrinsic Fluorescence, ChemBioChem. 14 (2013) 846–850, https://doi.org/10.1002/cbic.201300103.
[19] C.W. Chung, A.D. Stephens, E. Ward, Y. Feng, M.J. Davis, C.F. Kaminski, G. S. Kaminski Schierle, Label-Free Characterization of Amyloids and Alpha-Synuclein Polymorphs by Exploiting Their Intrinsic Fluorescence Property, Anal. Chem. 94 (2022) 5367–5374, https://doi.org/10.1021/acs.analchem.1c05651.
[20] O. Tcherkasskaya, Photo-activity induced by amyloidogenesis, Protein Sci. 16 (2007) 561–571, https://doi.org/10.1110/ps.062578307.
[21] G. Rosenman, N. Amdursky, M. Molotskii, D. Aronov, L. Adler-Abramovich, E. Gazit, Blue luminescence based on quantum confinement at peptide nanotubes, Nano Lett. 9 (2009) 3111–3115, https://doi.org/10.1021/nl9008265.
[22] P. Hanczyc, M. Samoc, B. Norden, Multiphoton absorption in amyloid protein fibres, Nat. Photonics. 7 (2013) 969–972, https://doi.org/10.1038/nphoton.2013.282.
[23] D. Pinotsi, L. Grisanti, P. Mahou, R. Gebauer, C.F. Kaminski, A. Hassanali, G. S. Kaminski Schierle, Proton Transfer and Structure-Specific Fluorescence in Hydrogen Bond-Rich Protein Structures, J. Am. Chem. Soc. 138 (2016) 3046–3057, https://doi.org/10.1021/jacs.5b11012.
[24] L. Grisanti, D. Pinotsi, R. Gebauer, G.S. Kaminski Schierle, A.A. Hassanali, A computational study on how structure influences the optical properties in model crystal structures of amyloid fibrils, Phys. Chem. Chem. Phys. 19 (2017) 4030–4040, https://doi.org/10.1039/c6cp07564a.
[25] A.D. Stephens, M.N. Qaisrani, M.T. Ruggiero, G.D. Mirón, U.N. Morzan, M. C. González Lebrero, S.T.E. Jones, E. Poli, A.D. Bond, P.J. Woodhams, E.M. Kleist, L. Grisanti, R. Gebauer, J.A. Zeitler, D. Credgington, A. Hassanali, G.S. Kaminski Schierle, Short hydrogen bonds enhance nonaromatic protein-related fluorescence, Proc. Natl. Acad. Sci. U. S. A. 118 (2021), https://doi.org/10.1073/pnas.2020389118.
[26] R. Ye, Y. Liu, H. Zhang, H. Su, Y. Zhang, L. Xu, R. Hu, R.T.K. Kwok, K.S. Wong, J.W. Y. Lam, W.A. Goddard, B.Z. Tang, Non-conventional fluorescent biogenic and synthetic polymers without aromatic rings, Polym. Chem. 8 (2017) 1722–1727, https://doi.org/10.1039/c7py00154a.
[27] L.L. Del Mercato, P.P. Pompa, G. Maruccio, A. Della Torre, S. Sabella, A. M. Tamburro, R. Cingolani, R. Rinaldi, Charge transport and intrinsic fluorescence in amyloid-like fibrils, Proc. Natl. Acad. Sci. U. S. A. 104 (2007) 18019–18024, https://doi.org/10.1073/pnas.0702843104.
[28] S. Prasad, I. Mandal, S. Singh, A. Paul, B. Mandal, R. Venkatramani, R. Swaminathan, Near UV-Visible electronic absorption originating from charged amino acids in a monomeric protein, Chem. Sci. 8 (2017) 5416–5433, https://doi.org/10.1039/c7sc00880e.
[29] H.A.M. Ardona, E.R. Draper, F. Citossi, M. Wallace, L.C. Serpell, D.J. Adams, J. D. Tovar, Kinetically Controlled Coassembly of Multichromophoric Peptide Hydrogelators and the Impacts on Energy Transport, J. Am. Chem. Soc. 139 (2017) 8685–8692, https://doi.org/10.1021/jacs.7b04006.
[30] K.H. Jong, Y.T. Azar, L. Grisanti, A.D. Stephens, S.T.E. Jones, D. Credgington, G. S. Kaminski Schierle, A. Hassanali, Low energy optical excitations as an indicator of structural changes initiated at the termini of amyloid proteins, Phys. Chem. Chem. Phys. 21 (2019) 23931–23942, https://doi.org/10.1039/c9cp04648h.
[31] A. Kumar, D. Ahari, A. Priyadarshi, M. Ziauddin Ansari, R. Swaminathan, Weak Intrinsic Luminescence in Monomeric Proteins Arising from Charge Recombination, J. Phys. Chem. B. 124 (2020) 2731–2746, https://doi.org/10.1021/acs.jpcb.9b10071.
[32] S. Shaham-Niv, Z.A. Arnon, D. Sade, A. Lichtenstein, E.A. Shirshin, S. Kolusheva, E. Gazit, Intrinsic Fluorescence of Metabolite Amyloids Allows Label-Free Monitoring of Their Formation and Dynamics in Live Cells, Angew. Chemie - Int. Ed. 57 (2018) 12444–12447, https://doi.org/10.1002/anie.201806565.
[33] Z.A. Arnon, T. Kreiser, B. Yakimov, N. Brown, R. Aizen, S. Shaham-Niv, P. Makam, M.N. Qaisrani, E. Poli, A. Ruggiero, I. Slutsky, A. Hassanali, E. Shirshin, D. Levy, E. Gazit, On-off transition and ultrafast decay of amino acid luminescence driven by modulation of supramolecular packing, Iscience. 24 (2021), https://doi.org/10.1016/j.isci.2021.102695.
[34] M. Grelich-Mucha, A.M. Garcia, V. Torbeev, K. Ożga, Ł. Berlicki, J. Olesiak-Bańska, Autofluorescence of Amyloids Determined by Enantiomeric Composition of Peptides, J. Phys. Chem. B. (2021), https://doi.org/10.1021/acs.jpcb.1c00808.
[35] X. Ren, Q. Zou, C. Yuan, R. Chang, R. Xing, X. Yan, The Dominant Role of Oxygen in Modulating the Chemical Evolution Pathways of Tyrosine in Peptides: Dityrosine or Melanin, Angew. Chemie - Int. Ed. 58 (2019) 5872–5876, https://doi.org/10.1002/anie.201814575.
[36] A. Fricano, F. Librizzi, E. Rao, C. Alfano, V. Vetri, Blue autofluorescence in protein aggregates "lighted on" by UV induced oxidation, Biochim. Biophys. Acta - Proteins Proteomics. 1867 (2019), https://doi.org/10.1016/j.bbapap.2019.07.011.
[37] Z. Wygralak, K. Sylwia, P. Bezara, Deep blue autofluorescence reflects the oxidation state of human transthyretin, Redox Biol. 56 (2022), https://doi.org/10.1016/j.redox.2022.102434.
[38] A. Shukla, S. Mukherjee, S. Sharma, V. Agrawal, K.V.R. Kishan, P. Guptasarma, A novel UV laser-induced visible blue radiation from protein crystals and aggregates: Scattering artifacts or fluorescence transitions of peptide electrons delocalized through hydrogen bonding? Arch. Biochem. Biophys. 428 (2004) 144–153, https://doi.org/10.1016/j.abb.2004.05.007.
[39] L. Sobczyk, S. Grabowki, T.M. Krygowksi, Interrelation between H-Bond and Pi-Electron Delocalization, Chem. Rev. 105 (2005) 3513–3560, https://doi.org/10.1021/cr030083c.
[40] S. Sharpe, K. Simonetti, J. Yau, P. Walsh, Solid-state NMR characterization of autofluorescent fibrils formed by the elastin-derived peptide GVGVAGVG, Biomacromolecules. 12 (2011) 1546–1555, https://doi.org/10.1021/bm101486s.
[41] I. Sirangelo, M. Borriello, G. Irace, C. Ianuzzi, Intrinsic blue-green fluorescence in amyloyd fibrils, AIMS Biophys. 5 (2018) 155–165, https://doi.org/10.3934/biophy.2018.2.155.
[42] L. Grisanti, M. Sapunar, A. Hassanali, N. Došlić, Toward Understanding Optical Properties of Amyloids: A Reaction Path and Nonadiabatic Dynamics Study, J. Am. Chem. Soc. 142 (2020) 18042–18049, https://doi.org/10.1021/jacs.0c07134.
[43] C. Niyangoda, T. Miti, L. Breydo, V. Uversky, M. Muschol, Carbonyl-based blue autofluorescence of proteins and amino acids, PLoS One. 12 (2017), https://doi.org/10.1371/journal.pone.0176983.
[44] C. Iannuzzi, M. Borriello, M. Portaccio, G. Irace, I. Sirangelo, Insights into insulin fibril assembly at physiological and acidic pH and related amyloid intrinsic fluorescence, Int. J. Mol. Sci. 18 (2017), https://doi.org/10.3390/ijms18122551.
[45] A. Monti, C. Bruckmann, F. Blasi, M. Ruvo, L. Vitagliano, N. Doti, Amyloid-like Prep1 peptides exhibit reversible blue-green-red fluorescencein vitro and in living cells, Chem. Commun. 57 (2021) 3720–3723, https://doi.org/10.1039/d1cc01145f.
[46] M. Žganec, A.T. Vercic, M. Igor, M. Škarabot, E. Žerovnik, Amyloid Fibrils of Stefin B Show Anisotropic Properties, Int. J. Mol. Sci. 24 (2023), https://doi.org/10.3390/ijms24043737.
[47] B. Apter, N. Lapshina, I. Lapsker, A. Handelman, A. Accardo, C. Diaferia, G. Morelli, G. Rosenman, Fold-Sensitive Visible Fluorescence in β-Sheet Peptide Structures, Adv. Opt. Mater. 9 (2021), https://doi.org/10.1002/adom.202002247.
[48] E. Wieczorek, P. Bezara, A. Ożyhar, Deep blue autofluorescence reveals the instability of human transthyretin, Int. J. Biol. Macromol. 191 (2021) 492–499, https://doi.org/10.1016/j.ijbiomac.2021.09.107.
[49] T. Leyder, J. Mignon, D. Mottet, C. Michaux, Unveiling the Metal-Dependent Aggregation Properties of the C- terminal Region of Amyloidogenic Intrinsically Disordered Protein Isoforms DPF3b and DPF3a C-terminal Region of Amyloidogenic Intrinsically Disordered, Int. J. Mol. Sci. 23 (2022), https://doi.org/10.3390/ijms232315291.
[50] C. Diaferia, C. Schiattarella, E. Gallo, B. Della Ventura, G. Morelli, R. Velotta, L. Vitagliano, A. Accardo, Fluorescence Emission of Self-assembling Amyloid-like Peptides: Solution versus Solid State, ChemPhysChem. 22 (2021) 2215–2221, https://doi.org/10.1002/cphc.202100570.
[51] H. Cui, J. Schlesinger, S. Schoenhals, M. Tönjes, I. Dunkel, D. Meierhofer, E. Cano, K. Schulz, M.F. Berger, T. Haack, S. Abdelilah-Seyfried, M.L. Bulyk, S. Sauer, S. R. Sperling, Phosphorylation of the chromatin remodeling factor DPF3a induces cardiac hypertrophy through releasing HEY repressors from DNA, Nucleic Acids Res. 44 (2015) 2538–2553, https://doi.org/10.1093/nar/gkv1244.
[52] W. Guanglei, W. Bingbing, Y. Peixin, Epigenetics in Congenital Heart Disease, J. Am. Heart Assoc. 11 (2022), https://doi.org/10.1161/JAHA.121.025163.
[53] J. Mignon, T. Leyder, C. Michaux, The intrinsically disordered DPF3 zinc finger protein: a promising new target in cancer therapy, J. Cancer Biol. 3 (2022) 79–82, https://doi.org/10.46439/cancerbiology.3.44.
[54] E.M. Blalock, J.W. Geddes, K.C. Chen, N.M. Porter, W.R. Markesbery, P. W. Landfield, Incipient Alzheimer's disease: Microarray correlation analyses reveal major transcriptional and tumor suppressor responses, Proc. Natl. Acad. Sci. U. S. A. 101 (2004) 2173–2178, https://doi.org/10.1073/pnas.0308512100.
[55] J.I. Satoh, Molecular network analysis of human microRNA targetome: From cancers to Alzheimers disease, BioData Min. 5 (2012), https://doi.org/10.1186/1756-0381-5-17.
[56] E.A. Rudnitskaya, A.O. Burnyasheva, T.A. Kozlova, D.A. Peunov, N.G. Kolosova, N. A. Stefanova, Changes in Glial Support of the Hippocampus during the Development of an Alzheimer's Disease-like Pathology and Their Correction by Mitochondria-Targeted Antioxidant SkQ1, Int. J. Mol. Sci. 23 (2022), https://doi.org/10.3390/ijms23031134.
[57] M. Huang, L. Xu, J. Liu, P. Huang, Y. Tan, S. Chen, Cell-Cell Communication Alterations via Intercellular Signaling Pathways in Substantia Nigra of Parkinson's Disease, Front. Aging Neurosci. 14 (2022), https://doi.org/10.3389/fnagi.2022.828457.

[58] J. Mignon, D. Mottet, G. Verrillo, A. Matagne, E.A. Perpète, C. Michaux, Revealing Intrinsic Disorder and Aggregation Properties of the DPF3a Zinc Finger Protein, ACS Omega. 6 (2021) 18793–18801, https://doi.org/10.1021/acsomega.1c01948.
[59] J. Mignon, D. Mottet, T. Leyder, V.N. Uversky, E.A. Perpète, C. Michaux, Structural characterisation of amyloidogenic intrinsically disordered zinc finger protein isoforms DPF3b and DPF3a, Int. J. Biol. Macromol. 218 (2022) 57–71, https://doi.org/10.1016/j.ijbiomac.2022.07.102.
[60] B.J.H. Kuipers, H. Gruppen, Prediction of molar extinction coefficients of proteins and peptides using UV absorption of the constituent amino acids at 214 nm to enable quantitative reverse phase high-performance liquid chromatography-mass spectrometry analysis, J. Agric. Food Chem. 55 (2007) 5445–5451, https://doi.org/10.1021/jf070337l.
[61] J. Jumper, R. Evans, A. Pritzel, T. Green, M. Figurnov, O. Ronneberger, K. Tunyasuvunakool, R. Bates, A. Žídek, A. Potapenko, A. Bridgland, C. Meyer, S.A. A. Kohl, A.J. Ballard, A. Cowie, B. Romera-Paredes, S. Nikolov, R. Jain, J. Adler, T. Back, S. Petersen, D. Reiman, E. Clancy, M. Zielinski, M. Steinegger, M. Pacholska, T. Berghammer, S. Bodenstein, D. Silver, O. Vinyals, A.W. Senior, K. Kavukcuoglu, P. Kohli, D. Hassabis, Highly accurate protein structure prediction with AlphaFold, Nature. 596 (2021) 583–589, https://doi.org/10.1038/s41586-021-03819-2.
[62] M. Mirdita, K. Schütze, Y. Moriwaki, L. Heo, S. Ovchinnikov, M. Steinegger, ColabFold: making protein folding accessible to all, Nat. Methods. 19 (2022) 679–682, https://doi.org/10.1038/s41592-022-01488-1.
[63] M.H.M. Olsson, C.R. Søndergaard, M. Rostkowski, J.H. Jensen, PROPKA3: Consistent Treatment of Internal and Surface Residues in Empirical pKa Predictions, J. Chem. Theory Comput. 7 (2011) 525–537, https://doi.org/10.1021/ct100578z.
[64] C.R. Søndergaard, M.H.M. Olsson, M. Rostkowski, J.H. Jensen, Improved Treatment of Ligands and Coupling Effects in Empirical Calculation and Rationalization of pKa Values, J. Chem. Theory Comput. 7 (2011) 2284–2295, https://doi.org/10.1021/ct200133y.
[65] T.J. Dolinsky, P. Czodrowski, H. Li, J.E. Nielsen, J.H. Jensen, G. Klebe, N.A. Baker, PDB2PQR: Expanding and upgrading automated preparation of biomolecular structures for molecular simulations, Nucleic Acids Res. 35 (2007) 522–525, https://doi.org/10.1093/nar/gkm276.
[66] E. Jurrus, D. Engel, K. Star, K. Monson, J. Brandi, L.E. Felberg, D.H. Brookes, L. Wilson, J. Chen, K. Liles, M. Chun, P. Li, D.W. Gohara, T. Dolinsky, R. Konecny, D.R. Koes, J.E. Nielsen, T. Head-Gordon, W. Geng, R. Krasny, G.W. Wei, M.J. Holst, J.A. McCammon, N.A. Baker, Improvements to the APBS biomolecular solvation software suite, Protein Sci. 27 (2018) 112–128, https://doi.org/10.1002/pro.3280.
[67] N.A. Baker, D. Sept, S. Joseph, M.J. Holst, J.A. McCammon, Electrostatics of nanosystems: Application to microtubules and the ribosome, Proc. Natl. Acad. Sci. U. S. A. 98 (2001) 10037–10041, https://doi.org/10.1073/pnas.181342398.
[68] S. Unni, Y. Huang, R.M. Hanson, M. Tobias, S. Krishnan, W.W. Li, J.E. Nielsen, N. A. Baker, Web Servers and Services for Electrostatics Calculations with APBS and PDB2PQR, J. Comput. Chem. 32 (2011) 1488–1491, https://doi.org/10.1002/jcc.
[69] A. Hatos, J.M.C. Teixeira, S. Barrera-Vilarmau, A. Horvath, S.C.E. Tosatto, M. Vendruscolo, M. Fuxreiter, FuzPred: a web server for the sequence-based prediction of the context-dependent binding modes of proteins, Nucleic Acids Res 51 (2023), https://doi.org/10.1093/nar/gkad214.
[70] A. Hatos, S.C.E. Tosatto, M. Vendruscolo, M. Fuxreiter, FuzDrop on AlphaFold: visualizing the sequence-dependent propensity of liquid-liquid phase separation and aggregation of proteins, Nucleic Acids Res. 50 (2022) 337–344, https://doi.org/10.1093/nar/gkac386.
[71] K. Michael, Characterization of electronic transitions in complex molecules, Discuss. Faraday Soc. 9 (1950) 14–19, https://doi.org/10.1039/DF9500900014.
[72] J.C. Del Valle, J. Catalán, Kasha's rule: a reappraisal, Phys. Chem. Chem. Phys. 21 (2019) 10061–10069, https://doi.org/10.1039/c9cp00739c.
[73] A. Chattopadhyay, S. Haldar, Dynamic insight into protein structure utilizing red edge excitation shift, Acc. Chem. Res. 47 (2014) 12–19, https://doi.org/10.1021/ar400006z.
[74] S.M. Raja, S.S. Rawat, A. Chattopadhyay, A.K. Lala, Localization and environment of tryptophans in soluble and membrane- bound states of a pore-forming toxin from Staphylococcus aureus, Biophys. J. 76 (1999) 1469–1479, https://doi.org/10.1016/S0006-3495(99)77307-8.
[75] D.A.M. Catici, H.E. Amos, Y. Yang, J.M.H. van den Elsen, C.R. Pudney, The red edge excitation shift phenomenon can be used to unmask protein structural ensembles: implications for NEMO–ubiquitin interactions, FEBS J. 283 (2016) 2272–2284, https://doi.org/10.1111/febs.13724.
[76] P.K. Johansson, P. Koelsch, Label-free imaging of amyloids using their intrinsic linear and nonlinear optical properties, Biomed, Opt. Express. 8 (2017) 743–756, https://doi.org/10.1364/boe.8.000743.
[77] J. Pansieri, V. Josserand, S.J. Lee, A. Rongier, D. Imbert, M.M. Sallanon, E. Kövari, T.G. Dane, C. Vendrely, O. Chaix-Pluchery, M. Guidetti, J. Vollaire, A. Fertin, Y. Usson, P. Rannou, J.L. Coll, C. Marquette, V. Forge, Ultraviolet–visible–near-infrared optical properties of amyloid fibrils shed light on amyloidogenesis, Nat. Photonics. 13 (2019) 473–479, https://doi.org/10.1038/s41566-019-0422-6.
[78] S.I. Vavilov, Xxix., The dependence of the intensity of the fluorescence of dyes upon the wave-length of the exciting light, London, Edinburgh, Dublin Philos. Mag. J. Sci. 43 (1922) 307–320, https://doi.org/10.1080/14786442208565217.
[79] C. Diaferia, T. Sibillano, D. Altamura, V. Roviello, L. Vitagliano, C. Giannini, G. Morelli, A. Accardo, Structural Characterization of PEGylated Hexaphenylalanine Nanostructures Exhibiting Green Photoluminescence Emission, Chem. - A Eur. J. 23 (2017) 14039–14048, https://doi.org/10.1002/chem.201703055.
[80] A. Monti, C. Bruckmann, F. Blasi, M. Ruvo, L. Vitagliano, N. Doti, Amyloid-like Prep1 peptides exhibit reversible blue-green-red fluorescencein vitroand in living cells, Chem. Commun. 57 (2021) 3720–3723, https://doi.org/10.1039/d1cc01145f.
[81] J.R. Lakowicz, S. Keating-Nakamoto, Red edge Excitation of Fluorescence and Dynamic Properties of Proteins and Membranes, Biochemistry. 23 (1984) 3013–3021, https://doi.org/10.1021/bi00308a026.
[82] A.P. Demchenko, The red edge effects: 30 years of exploration, Luminescence. 17 (2002) 19–42, https://doi.org/10.1002/bio.671.
[83] M.F. Perutz, J.T. Finch, J. Berriman, A. Lesk, Amyloid fibers are water-filled nanotubes, Proc. Natl. Acad. Sci. U. S. A. 99 (2002) 5591–5595, https://doi.org/10.1073/pnas.042681399.
[84] T. Wang, H. Jo, W.F. DeGrado, M. Hong, Water Distribution, Dynamics, and Interactions with Alzheimer's β-Amyloid Fibrils Investigated by Solid-State NMR, J. Am. Chem. Soc. 139 (2017) 6242–6252, https://doi.org/10.1021/jacs.7b02089.
[85] A.P. Demchenko, V.I. Tomin, P.T. Chou, Breaking the Kasha Rule for More Efficient Photochemistry, Chem. Rev. 117 (2017) 13353–13381, https://doi.org/10.1021/acs.chemrev.7b00110.
[86] M.A. Saraiva, Interpretation of α-synuclein UV absorption spectra in the peptide bond and the aromatic regions, J. Photochem. Photobiol. B Biol. 212 (2020), https://doi.org/10.1016/j.jphotobiol.2020.112022.
[87] M. Gonnelli, G.B. Strambini, Phosphorescence lifetime of tryptophan in proteins, Biochemistry. 34 (1995) 13847-13857. https://doi.org.10.1021/bi00042a017.
[88] J. Chavez, L. Ceresa, J.M. Reeks, Y.M. Strzhemechny, J. Kimball, E. Kitchner, Z. Gryczynski, I. Gryczynski, Methods Appl. Fluoresc. 10 (2022), https://doi.org/10.1088/2050-6120/ac4c9a.
[89] J.M. Vanderkooi, D.B. Calhoun, S.W. Englander, On the Prevalence of Room-Temperature Protein Phosphorescence, Science. 236 (1987) 568–569, https://doi.org/10.1126/science.3576185.
[90] M. Gonnelli, G.B. Strambini, Intramolecular Quenching of Tryptophan Phosphorescence in Short Peptides and Proteins, Photochem. Photobiol. 81 (2005) 614–622, https://doi.org/10.1111/j.1751-1097.2005.tb00234.x.